1985ApJS...58...39B

THE ASTROPHYSICAL JOURNAL SUPPLEMENT SERIES, 58:39–66, 1985 May

SELF-SIMILAR SECONDARY INFALL AND ACCRETION IN AN EINSTEIN–DE SITTER UNIVERSE

EDMUND BERTSCHINGER
Princeton University Observatory; and Department of Astronomy, University of Virginia

Received 1984 January 3; accepted 1984 November 15

ABSTRACT

Similarity solutions have been found for secondary infall and accretion onto an initially overdense perturbation in an Einstein–de Sitter ($\Omega = 1$) universe. After the initial collapse of a positive density perturbation, bound shells continue to turn around and fall in, with the radius of the shell currently turning around increasing as $t^{8/9}$ and the mass within this radius increasing as $t^{2/3}$. The secondary infall approaches a self-similar form, with the exact behavior depending on the kind of gas and on central boundary conditions. If there is a central black hole, it grows by accretion, with the density having the power-law form $\rho \propto r^{-1.5}$ near the center. If there is no central black hole, a $\rho \propto r^{-2.25}$ density profile results, with infalling matter added to successively larger radii.

Solutions are given here for collisional, collisionless, and mixed gases. The collisional component, if present, accretes through an outwardly propagating shock, with fluid elements coming to rest a finite distance from the center if the adiabatic exponent $\gamma > 4/3$; softer equations of state may lead to black hole formation. The collisionless gas passes through the center and crosses itself, leading to the formation of outwardly propagating caustics. Each infalling collisionless particle relaxes after several crossing times to a periodic orbit given by the particle's own initial conditions, allowing galaxy and cluster halos formed by secondary infall to be dated. Since infall ceases when $\Omega \ll 1$, a galaxy halo of mass $10^{12}\ M_\odot$ within 100 kpc (for $H_0 = 100$ km s^{-1} Mpc^{-1}) can form only if $\Omega_0 \gtrsim 0.29$. The close relationship between clusters of galaxies and giant voids is discussed in light of the similarity solutions found here and those found previously for voids.

Subject headings: black holes — cosmology — galaxies: clustering — galaxies: formation — galaxies: structure — hydrodynamics

I. INTRODUCTION

The possibility that secondary infall of matter onto already formed galaxies might be able to produce halo density distributions $\rho \propto r^{-2} - r^{-3}$ was first recognized by Gott (1975) and Gunn (1977). If infall produces density profiles as shallow as r^{-2}, then the flat rotation curves of disk galaxies (Rubin, Ford, and Thonnard 1980) and the related observation of increasing mass-to-light ratio M/L on large scales might thereby be explained. A somewhat steeper r^{-3} profile resulting from infall could explain the Hubble law light profiles of elliptical galaxies (Gott 1975). There is thus considerable interest concerning the exact slope produced by secondary infall.

A simple model of infall, where mass shells are artificially halted at some constant fraction of their radius of maximum expansion ("turnaround radius"), predicts a density distribution $\rho \propto r^{-2.25}$ (Gott 1975; Gunn 1977). The question usually addressed in discussions of secondary infall is whether this profile can actually be attained once relaxation is included. Numerical simulations using spherical shell codes (Gott 1975; Pryor and Lecar 1983) have produced r^{-3} profiles, but theoretical arguments (Gunn 1977) and an N-body simulation (Dekel, Kowitt, and Shaham 1981) suggest that $\rho \propto r^{-2.25}$ is correct.

Gunn suggested that the infall process may become self-similar, i.e., unchanging in form and appearance, when lengths are scaled in terms of the current turnaround radius. He argued that under such conditions the relaxation may be expected to settle down sufficiently that the $r^{-2.25}$ density profile is obtained.

This paper demonstrates that Gunn's suggestion of self-similarity is correct, by deriving the similarity solution for secondary infall of a collisionless gas. It will be shown that the density profile $\rho \propto r^{-2.25}$ is indeed correct provided only that the initial density perturbation has finite mass excess as $r \to \infty$. Analytic and semianalytic methods are used, so the results are not subject to the uncertainties inherent in numerical simulations (cf. Dekel, Kowitt, and Shaham 1981). Investigation of the solutions provides a rich understanding of the relaxation and other processes leading to the power law $\rho \propto r^{-2.25}$ and other interesting features of the solution.

Fillmore and Goldreich (1984) have independently derived the collisionless similarity solution found here and its counterparts in planar and cylindrical geometry; this paper takes a slightly different approach not restricted to a collisionless gas.

Discussions of secondary infall have usually been restricted to collisionless particles, perhaps because hydrodynamics is more difficult to simulate numerically, but similarity solutions are given in this paper for both collisionless and collisional gases. In almost all cases the $\rho \propto r^{-2.25}$ profile results. The one different case is where a black hole in the center accretes the gas, leading to $\rho \propto r^{-1.5}$ if the gas falls freely into the black hole. An analytic solution is given for this case. It is hoped that the solutions and their physical interpretation given in this paper will put to rest doubts that a $\rho \propto r^{-2.25}$ density profile is produced by secondary infall, so long as $\Omega \approx 1$. (This restriction is not unreasonable since if $\Omega < 1$, there is a last bound shell and infall stops. The similarity solutions given below are approximately valid up to this time, and it will be shown that in any case the $r^{-2.25}$ profile formed earlier is preserved for a collisionless gas after infall ceases.)

All of the solutions given in this paper share the same initial conditions and linear and initial nonlinear evolution, which will be described now. Consider a sphere of radius R_i with a uniform overdensity $\delta\rho/\rho = \delta_i \ll 1$ at cosmic time t_i, embedded in an otherwise $\Omega = 1$ (Einstein–de Sitter) universe. That is, the initial density distribution is

$$\rho = \frac{1}{6\pi G t_i^2}\begin{cases} 1+\delta_i, & r < R_i; \\ 1, & r > R_i; \end{cases} \tag{1.1}$$

where $r = 0$ is the center of the sphere. The perturbation scale R_i is assumed to be much greater than the Jeans length, so that the gas may be taken to be pressureless, at least until a collapse occurs. It is convenient for the discussion, but not necessary for the conclusions, that the density be discontinuous. It is also convenient to take the Hubble flow to be unperturbed, $v = H_i r$, with $H_i = 2/(3t_i)$. It will be shown below that perturbing the velocity field does not change the self-similar evolution (although it does change the linear growth) provided the resulting perturbation in kinetic energy ΔT does not increase with radius faster than r^2 for $r > R_i$. (If the Hubble flow is perturbed only inside R_i, then $\Delta T \propto r^0$.) Heuristically, all information about the initial conditions except that preserved by global conservation laws (mass and energy) is "forgotten" by the fluid as the motion becomes self-similar, so it is unnecessary to worry about the details of the initial conditions.

As the universe expands, because of its higher density the matter inside R_i is decelerated more than that outside, further increasing the density contrast. The density inside R_i may be written $\rho = [1+\delta(\tau)]\rho_{\rm H}$, where $\tau = t/t_i$ is the cosmic time in units of the initial fiducial time, $\rho_{\rm H} = (6\pi G t^2)^{-1}$ is the Einstein–de Sitter density, and in the linear regime ($\delta \ll 1$; cf. Peebles 1980)

$$\delta(\tau) = \delta_i\left(\frac{3}{5}\tau^{2/3} + \frac{2}{5}\tau^{-1}\right). \tag{1.2}$$

Both growing and decaying modes are present because the Hubble flow is initially unperturbed. If the velocity is perturbed initially to $v = (1-\delta_i/3)H_i r$ for $r < R_i$, then only the growing mode is present; i.e., $\delta(\tau) = \delta_i \tau^{2/3}$. In either case the perturbation becomes nonlinear when $\delta \approx 1$, or $\tau \approx \delta_i^{-3/2}$.

As the density contrast grows, the matter initially inside R_i is increasingly decelerated. Eventually it ceases expanding altogether and turns around to recollapse. This event marks the transition to the nonlinear regime and occurs at a time

$$t_{\rm ita} = \frac{3\pi}{4}\delta_i^{-3/2} t_i, \tag{1.3}$$

if the Hubble flow is initially unperturbed; if only the growing mode is present initially, then δ_i should be replaced by $(5/3)\delta_i$. (Subscript ita stands for "initial turnaround" and is used here to distinguish $t_{\rm ita}$ from the turnaround time $t_{\rm ta}$ of more distant mass shells; see § II.) The maximum radius of the comoving shell initially at $r = R_i$ is

$$r_{\rm ita} = R_i \delta_i^{-1}, \tag{1.4}$$

with the same remarks holding about δ_i as for equation (1.3). The density interior to this mass shell is uniform until collapse and has a value at $t = t_{\rm ita}$ of

$$\rho_{\rm ta} = \left(\frac{3\pi}{4}\right)^2 \rho_{\rm H}. \tag{1.5}$$

Perturbing the initial Hubble flow changes the turnaround time and radius but not the density contrast. Outside $r_{\rm ita}$, the density decreases smoothly to $\rho_{\rm H}$ as $r \to \infty$.

After the first mass shells turn around, the matter in the overdense region collapses. If the collapse remains spherically symmetric, the central density becomes infinite at a nondimensional time

$$t_{\rm coll} = 2t_{\rm ita}. \tag{1.6}$$

Lin, Mestel, and Shu (1965) showed that even an infinitesimal deviation from spherical symmetry is magnified during a uniform collapse, so that collapse is more likely to occur in a plane or along a line than at a point. This should not affect the self-similarity sufficiently far from the origin, since the self-similar scale length increases with time (although tidal torques from other overdense regions may cause growing deviations from spherical symmetry); moreover, spherical symmetry may be preserved for collapse in a centrally condensed mass distribution (Goodman and Binney 1983). The assumption of spherical infall cannot be rigorously justified without detailed numerical calculations of the collapse of nonspherical perturbations. Even if spherical symmetry proves to be a poor assumption, however, it is adopted here because it leads to analytic and semianalytic solutions which may give insight into processes also important in nonspherical infall.

After collapse occurs, the fluid motion depends on central boundary conditions and on whether the fluid is collisionless or collisional ("dissipationless" or "dissipative"). In all cases, however, the fluid motion becomes self-similar at late times, provided additional physical processes (e.g., cooling) do not introduce additional scales. Physically the self-similarity arises because mass shells outside the initially overdense shells are also bound and turn around at successively later times for more distant shells, with the turnaround radius increasing as $t^{8/9}$ and providing the only scale length.

This paper gives solutions for a variety of kinds of fluids and boundary conditions. The case of a central black hole quietly accreting all the infalling gas is considered first, in § II. If there is no central black hole and the gas is collisional, a shock forms and propagates outward; § III gives the similarity solutions for adiabatic postshock flow. Collisionless fluid shells do not shock; instead they pass right through each other and through the center. The motion still becomes self-similar, however, and the solution is given in § IV. The motion is in fact self-similar for an arbitrary mixture of collisionless and collisional fluids; § V gives the solution for an $\Omega \ll 1$ collisional fluid moving in the potential of the $\Omega = 1$ collisionless solution of § IV. The results are discussed and summarized in § VI. A comparison is made with similarity solutions found recently for expanding voids by Bertschinger (1985, hereafter Paper I); it is also shown how the collisionless similarity solutions can be used to infer the ages of objects formed by secondary infall; a lower limit on Ω_0 can thereby be obtained.

II. COLD ACCRETION ONTO A BLACK HOLE

The cold accretion solution given first is the simplest, both mathematically and physically, of the several self-similar infall solutions given in this paper. It is also the prototype for the rest of the solutions. Central boundary conditions are disposed of by placing a black hole in the center. The black hole mass equals, by assumption, the mass of fluid previously accreted. If gas accretes onto a preexisting black hole, e.g., a primordial black hole (Carr 1978)—perhaps the most likely scenario under which this solution applies—then the similarity solution becomes valid when the accreted mass dominates the initial black hole mass. The gas is self-gravitating (far outside the hole the gas motion is Einstein–de Sitter Hubble flow), although close to the center the integrated mass is dominated by the black hole. It will be shown below that no shell-crossing occurs, so the gas remains pressureless, assuming it is initially so. The resulting solution is clearly unrealistic sufficiently close to the black hole: the slightest amount of angular momentum will lead to an accretion disk, the radiation from which will heat the gas; general relativistic effects are neglected; etc. However, the solution will be valid far outside the black hole and at large distances matches the other solutions given below.

A Lagrangian description is adopted here for convenience. Consider a fluid element at radius $r = r_i > R_i$ at the initial time $t = t_i$, where R_i is the initial radius of the overdense region. The evolution for $r_i < R_i$ was discussed in § I; here we discuss the motion for $r_i > R_i$ after the first shells collapse (eq. [1.6]), so that the motion becomes self-similar. At cosmic time $t = \tau t_i$, the element being considered is at $r = y r_i$. Since there are no pressure forces, the trajectory of the fluid particle obeys Newton's law

$$\frac{d^2 r}{dt^2} = -\frac{Gm}{r^2}, \tag{2.1}$$

where

$$m = m(r_i) = \frac{4}{3}\pi\rho_i r_i^3\left(1 + \delta_i \frac{R_i^3}{r_i^3}\right) \equiv \frac{4}{3}\pi\rho_i r_i^3(1+\Delta) \tag{2.2}$$

is the fixed mass interior to the Lagrangian element [$\rho_i = 1/(6\pi G t_i^2)$ is the initial Einstein–de Sitter density]. The presence of the black hole in the center does not change equation (2.2), since the hole is assumed to have grown by accretion of the gas. Written in nondimensional form, equation (2.1) becomes

$$\ddot{y} = -\frac{2}{9}(1+\Delta)\frac{1}{y^2}, \tag{2.3}$$

where dots denote derivatives with respect to τ. Equation (2.3) can be integrated once to give

$$\frac{1}{2}\dot{y}^2 = \frac{2}{9}(1+\Delta)\frac{1}{y} - \frac{2}{9}\Delta, \tag{2.4}$$

where it has been assumed that $\dot{y} = \frac{2}{3}$ at $\tau = 1$; i.e., the Hubble flow is initially unperturbed outside R_i. A second integration by quadrature gives y implicitly:

$$\tau = \frac{3}{4}(\theta - \sin\theta)\Delta^{-3/2} \equiv d\Delta^{-3/2}, \tag{2.5}$$

valid for $\Delta \ll 1$, with

$$y\Delta \equiv \sin^2\frac{\theta}{2} \equiv \beta. \tag{2.6}$$

Interestingly, equations (2.5) and (2.6) apply also for particles moving outside uncompensated holes (i.e., voids; see Paper I), provided one makes the substitutions $\Delta \to -\Delta, \theta \to -\theta$, and $\sin\theta \to \sinh\theta$. This should not be too surprising, since uncompensated holes arise from initial conditions just the opposite of those assumed here (i.e., $\delta\rho/\rho < 0$ for $r_i < R_i$).

Although equation (2.5) was derived for a given mass shell, it applies for all mass shells, which may be distinguished by the mean relative mass excess Δ given by equation (2.2), so long as $\delta_i \ll 1$ and $r_i > R_i$. At fixed time τ, increasing r corresponds to increasing r_i and decreasing θ. The variable θ provides more than a convenient parameterization of the motion though since, as we will see below, at fixed θ the motion is constant aside from power-law scalings; i.e., the motion is self-similar.

From equation (2.4), the nondimensional radius of a fluid element turning around (i.e., having $\dot{y} = 0$) at time t is $y = \Delta^{-1}$ (cf. eq. [1.4]), corresponding to $\theta = \pi$ (eq. [2.6]). Using equations (2.2) and (2.5), the dimensional turnaround radius is, for $t \geq t_{\rm ita}$ (cf. eqs. [1.3] and [1.4]),

$$r_{\rm ta}(t) = r_{\rm ita}\left(\frac{t}{t_{\rm ita}}\right)^{8/9} = \left(\frac{3\pi}{4}\right)^{-8/9}\delta_i^{1/3}R_i\tau^{8/9}. \tag{2.7}$$

The first equality is true for almost arbitrary initial velocity perturbation (so long as the resulting energy $E[r]$ increases no faster than r^2). The second equality expresses the initial turnaround time $t_{\rm ita}$ and radius $r_{\rm ita}$ in terms of initial conditions for unperturbed Hubble flow (eqs. [1.3] and [1.4]). For initial Hubble flow with only the growing mode present, the second equality is correct if $\delta_i \to (5/3)\delta_i$. Thus after the first mass shells turn around, the turnaround radius increases as $t^{8/9}$. The mass within $r_{\rm ta}$ therefore grows as $t^{2/3}$; from equation (2.2),

$$m_{\rm ta}(t) = m_{\rm ta}(t_{\rm ita})\left(\frac{t}{t_{\rm ita}}\right)^{2/3} = \left(\frac{3\pi}{4}\right)^{-2/3}\frac{4}{3}\pi\delta_i\rho_i R_i^3\tau^{2/3}. \tag{2.8}$$

It is convenient in what follows to nondimensionalize the radius in terms of the turnaround radius:

$$\lambda \equiv \frac{r}{r_{\rm ta}(t)} = \lambda(\theta) = \beta\left(\frac{4d}{3\pi}\right)^{-8/9} = \sin^2\frac{\theta}{2}\left(\frac{\theta - \sin\theta}{\pi}\right)^{-8/9}, \tag{2.9}$$

where equations (2.2), (2.5), and (2.6) have been used in writing $\lambda = \lambda(\theta)$. The entire range in radius, $0 \le r, \lambda < \infty$, is spanned by $0 < \theta \le 2\pi$. When combined with equation (2.5), equation (2.9) gives the nondimensional trajectory $\lambda = \lambda(\theta[\tau])$ of a Lagrangian fluid particle, for which Δ is constant. Note from equation (2.5) that changing Δ (i.e., changing the Lagrangian coordinate) is equivalent to rescaling τ. Thus, when the time is properly scaled (so that, e.g., $\lambda = 1$ at $\tau = 1$), *all particles have the same nondimensional trajectory*. This is an important point which holds for all similarity solutions and will be discussed further below. Equations (2.5) and (2.9) show that λ is a single-valued function of τ, hence shell-crossing does not occur, as was assumed.

The trajectory is plotted in Figure 4 (*dashed curve*) in the form $r/r_{\rm ta}(t_{\rm ta}) \equiv r/r'_{\rm ta} = \lambda(t/t_{\rm ta})^{8/9}$ versus $t/t_{\rm ta}$, where $t_{\rm ta}$ and $r'_{\rm ta}$ are the turnaround time and radius for a given particle. Note from equation (2.9) that λ nondimensionalizes r using the *current* (time-varying) turnaround radius, while in Figure 4, r is nondimensionalized using the *fixed* turnaround radius of a specific particle; however, all particles have the same trajectory $r(t)$ when r and t are in units of the turnaround radius $r'_{\rm ta}$ and time $t_{\rm ta}$ of the particle. The portion of the trajectory for $t < t_{\rm ta}$ shows the motion before the particle first turns around and is given by equations (2.5) and (2.9) with $0 \le \theta < \pi$. The trajectory is symmetrical about $t = t_{\rm ta}$; the particle falls into the black hole at $t = 2t_{\rm ta}$ (cf. eq. [1.6]). For $t \ll t_{\rm ta}$, the trajectory is that of unperturbed Hubble flow, $r \propto t^{2/3}$.

Equation (2.7) may be derived heuristically up to a factor of order unity from energy conservation and dimensional analysis. This is a useful exercise since it shows the relation of the infall solutions to similarity solutions for expanding voids (Paper I); moreover, self-similarity relies in general on a scale length being provided by conserved quantities. From the initial conditions described in § I, the total energy inside a sphere of initial radius $r_i > R_i$ is

$$E(r_i) = -\frac{4\pi}{9}\frac{\rho_i R_i^5}{t_i^2}\delta_i\frac{r_i^2}{R_i^2}. \tag{2.10}$$

Now for $r \gg r_{\rm ta}$ the particle trajectories correspond closely to unperturbed Hubble flow, $r(t) = r_i(t/t_i)^{2/3}$. From equation (2.10) the energy within $r(t)$ is then

$$E(r,t) = -\frac{4\pi}{9}\frac{\rho_i R_i^3}{t_i^2}\delta_i r^2\tau^{-4/3}. \tag{2.11}$$

The quantities E, t, and $\rho_{\rm H}$ can be combined to form a unique length scale, which must by dimensional analysis approximately equal $r_{\rm ta}$; using equation (2.11) then gives

$$r_{\rm ta} \approx \left[\frac{-E(r_{\rm ta},t)t^2}{\rho_{\rm H}}\right]^{1/5} \Rightarrow r_{\rm ta}(t) \approx \delta_i^{1/3}R_i\tau^{8/9}. \tag{2.12}$$

Thus equation (2.7) can be derived from dimensional analysis, as expected for a similarity solution. Equations (2.10) and (2.11) also occur in the solutions for uncompensated holes (Paper I), but with opposite sign, since in the case of a hole there is a mass deficit (energy excess) rather than a mass excess (energy deficit). The sign change does not affect the dimensional analysis, however, so holes arising from similar initial conditions (but with $\delta_i < 0$) expand proportionately to the turnaround radius for an initial overdensity.

Equation (2.11) also shows why perturbing the Hubble flow initially inside R_i does not affect the similarity solution: the energy $\propto -r^2$, so any constant energy change becomes negligible at sufficiently large distances, or when the turnaround radius becomes large enough. Of course, if the density distribution (1.1) grows from a smaller perturbation in the past, the Hubble flow will also be perturbed outside R_i (i.e., requiring that there be only a growing mode perturbs the Hubble flow *everywhere*, although decreasingly as $r \to \infty$), in such a way that E in equation (2.11) is changed by a constant multiplicative factor of order unity. This will change the coefficient in the second equality of equation (2.7), but then the meanings of δ_i and R_i become less clear, since the initial "hatbox" density distribution has this shape only at the exact instant $t = t_i$. The first equality of equation (2.7) is correct as long as $E(r) \propto r^2$ for large r and thus is true for almost any initial perturbation with a finite mass excess as $r \to \infty$.

The fluid variables may now be determined as a function of the nondimensional radius λ. First, the fluid velocity is, from equations (2.4) and (2.5),

$$v = \frac{dr}{dt} = \frac{r}{t}\frac{\sin\theta(\theta - \sin\theta)}{(1-\cos\theta)^2} \equiv \frac{r_{\rm ta}(t)}{t}V(\lambda). \tag{2.13}$$

The velocity is written as a dimensional scale factor $r_{\rm ta}/t$ times a nondimensional function $V(\lambda)$. This separation follows from self-similarity: the fluid motion is unchanging when units are scaled appropriately in time (here, $r \to \lambda = r/r_{\rm ta}$, $v \to V = vt/r_{\rm ta}$). Self-similarity occurs in secondary infall because gravity has no preferred scales and the initial scale length R_i becomes unimportant as the turnaround radius progresses to larger comoving radii; $r_{\rm ta}$, t, and $\rho_{\rm H}$ (or G) then supply all the physical units.

The nondimensional velocity is plotted out to three turnaround radii as the solid curve in Figure 1*a*. The velocity is zero at $\lambda = 1$ ($r = r_{\rm ta}$) and approaches unperturbed Hubble

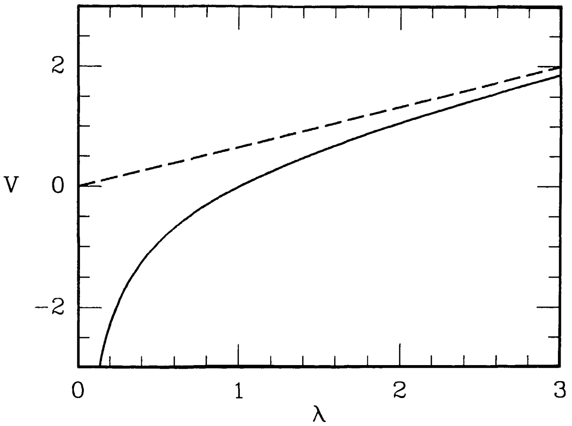

FIG. 1*a*

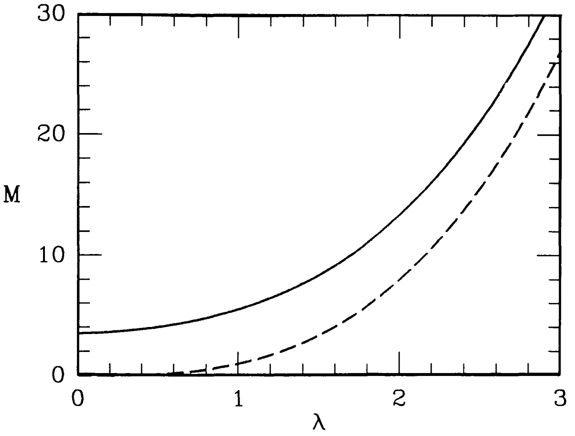

FIG. 1*b*

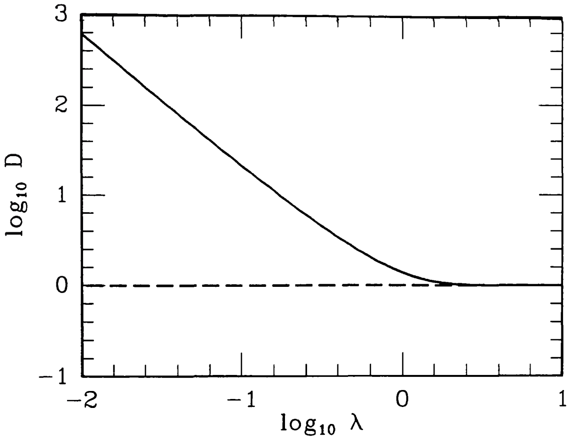

FIG. 1*c*

FIG. 1.—Nondimensionalized fluid distribution for pressureless self-similar accretion onto a black hole in an Einstein–de Sitter universe (*solid curves*), compared with unperturbed Hubble flow (*dashed curves*). The turnaround radius is $\lambda = 1$. (*a*) Velocity vs. radius (eq. [2.13]). (*b*) Mass vs. radius (eq. [2.15]). (*c*) Density vs. radius (eq. [2.21]).

flow $V = \frac{2}{3}\lambda$ (prevailing if there were no black hole or mass excess; see the dashed curve) for $\lambda \gg 1$. Close to the origin the velocity behaves as

$$V \approx -2^{-4/3}\pi\lambda^{-1/2}, \qquad \lambda \ll 1; \qquad (2.14)$$

as expected, $v \propto -r^{-1/2}$ for free fall onto a point mass.

The integrated mass interior to radius r is obtained using equations (2.2), (2.5), and (2.6). For $\Delta \ll 1$, they give

$$m = \tfrac{4}{3}\pi\rho_{\mathrm{H}} r^3 d^2 \beta^{-3} \equiv \tfrac{4}{3}\pi\rho_{\mathrm{H}} r_{\mathrm{ta}}^3 M(\lambda). \qquad (2.15)$$

Self-similarity is again evident from the factoring out of the time dependence from m, leaving the nondimensional $M(\lambda)$. The mass within a surface of constant λ thus increases as $t^{2/3}$. Equation (2.15) was given in a slightly different form in equation (19.48) of Peebles (1980). The $t^{2/3}$ time dependence of the accreted mass was first given by Gott (1975).

The nondimensional mass is plotted in Figure 1*b* (*solid curve*), where it is compared with the mass distribution for unperturbed Hubble flow (*dashed curve*), $M = \lambda^3$. There are two interesting things to notice. First, near the origin M approaches the constant value

$$M_{\mathrm{bh}} = M(0) = \left(\frac{3\pi}{4}\right)^2 2^{-2/3} \approx 3.497; \qquad (2.16)$$

this is the nondimensional mass of the central black hole. The dimensional black hole mass m_{bh} therefore grows as $t^{2/3}$. The turnaround radius and black hole mass are linked by equations (2.15) and (2.16); specifying one determines the other, since we have assumed that all of the accreted gas, and no more, goes into the hole.

The second interesting feature of the mass distribution is that as $\lambda \to \infty$,

$$M \approx \lambda^3\left(1 + \frac{3}{5}d^{2/3}\right) = \lambda^3 + \frac{3}{5}\left(\frac{3\pi}{4}\right)^{8/3} + O(\lambda^{-1}), \qquad \lambda \gg 1. \qquad (2.17)$$

Thus there is a finite total dimensional mass excess

$$m_x(t) \equiv \lim_{r \to \infty}\left[m(r,t) - \frac{4}{3}\pi\rho_{\mathrm{H}} r^3\right] = \frac{4}{5}\pi\left(\frac{3\pi}{4}\right)^{8/3}\rho_{\mathrm{H}} r_{\mathrm{ta}}^3. \qquad (2.18)$$

Note that this mass excess is greater than the black hole mass: $M_x = (3/5)(3\pi/4)^{8/3} \approx 5.898 > M_{\mathrm{bh}}$. For $t > t_{\mathrm{ita}}$, both m_{bh} and m_x are also greater than the initial mass deficit $\delta_i(4\pi/3)\rho_i R_i^3$. This seems at first paradoxical: how can a *constant* initial mass excess lead to a *growing* excess, especially one greater than the black hole mass? This paradox is resolved by noting that the initial excess perturbs the fluid trajectories instantaneously at all radii (assuming Newtonian gravity); since even distant mass shells are decelerated slightly more than if $\Omega = 1$ everywhere, there is a mass excess greater than the black hole mass. The black hole grows by accretion and hence so does the excess at large distances. Conservation of mass is not violated since m_x is the excess as $r \to \infty$, while mass conservation can only be applied to a finite volume; the Lagrangian formulation guarantees that mass is conserved locally. Self-similarity in fact demands that m_x and $m_{\rm bh}$ grow like $t^{2/3}$.

To obtain the density we follow the procedure of Paper I (eqs. [3.19]–[3.21]) and consider two different mass shells: one initially at r_i, and at r at time τ; the other initially at $r_i + dr_i$, and at $r + dr$ at τ. Mass conservation gives

$$\rho_i r_i^2\, dr_i = \rho r^2\, dr. \qquad (2.19)$$

Now from equation (2.5), $\tau = \tau(\Delta, y) = \tau(\Delta[r_i], r/r_i)$ gives the time at which a fluid shell originally at r_i has traveled to r. Since equation (2.19) refers to a fixed time τ, dr_i and dr are related by

$$0 = d\tau = \left(\frac{\partial\tau}{\partial\Delta}\frac{\partial\Delta}{\partial r_i} + \frac{\partial\tau}{\partial y}\frac{\partial y}{\partial r_i}\right) dr_i + \left(\frac{\partial\tau}{\partial\Delta}\frac{\partial\Delta}{\partial r} + \frac{\partial\tau}{\partial y}\frac{\partial y}{\partial r}\right) dr. \qquad (2.20)$$

Evaluating the partial derivatives at r, after some algebra we obtain

$$\rho = \rho_i \frac{r_i^2}{r^2}\frac{dr_i}{dr} = \rho_{\rm H}\frac{d^2\beta^{-3}}{1+3\chi} \equiv \rho_{\rm H} D(\lambda), \qquad \chi \equiv 1 - \frac{3}{2}\frac{V(\lambda)}{\lambda}. \qquad (2.21)$$

Because of self-similarity, the density at fixed λ is a constant times the Einstein–de Sitter (unperturbed Hubble) density $\rho_{\rm H}$ at that epoch.

The nondimensional density is plotted in Figure 1c; the dashed line gives the unperturbed density $D = 1$. From equation (2.21), at the turnaround radius the density is

$$D_{\rm ta} = D(1) = \left(\frac{3\pi}{8}\right)^2 \approx 1.388; \qquad (2.22)$$

from equation (2.15) the mean density interior to $r_{\rm ta}$ equals the nondimensional mass at $\lambda = 1$, or (cf. eq. [1.5])

$$M_{\rm ta} = \left(\frac{3\pi}{4}\right)^2 \approx 5.552. \qquad (2.23)$$

Near the origin the density diverges as

$$D \approx 2^{-7/3}\pi\lambda^{-3/2}, \qquad \lambda \ll 1. \qquad (2.24)$$

Equations (2.14) and (2.24) imply that there is a finite mass flux

$$\lim_{r\to 0} 4\pi r^2 \rho v = -\dot{m}(0) \qquad (2.25)$$

at the origin. Since the black hole is assumed to grow from accretion, it is necessary for consistency that $\dot{m}(0) = \dot{m}_{\rm bh} = \frac{2}{3} m_{\rm bh}/t$. Making this substitution into equation (2.25) and nondimensionalizing gives the condition

$$\lim_{\lambda\to 0} -\lambda^2 D V = \frac{2}{9} M_{\rm bh}. \qquad (2.26)$$

The reader may easily verify equation (2.26) using equations (2.14), (2.16), and (2.24).

For steady accretion, usually considered in astrophysics, equation (2.25) is valid everywhere, not just at $r = 0$. The cosmological accretion discussed here is not steady, yet there is a generalization of equations (2.25) and (2.26) which holds as long as mass shells do not cross:

$$M = -\frac{9}{2}\lambda^2 D\left(V - \frac{8}{9}\lambda\right), \qquad (2.27)$$

written in nondimensional form. Equation (2.27) gives an integral of the motion which holds for all values of λ. It may be derived directly from equations (2.13), (2.15), and (2.21); a derivation based on physical arguments is given in Bertschinger (1983).

Near the origin, the gas mass is negligible compared with $m_{\rm bh}$, so the gas is freely falling into the black hole. This situation is the same as that considered by Bondi (1952), inside his sonic radius. Bondi found the solution for steady, polytropic, non–self-gravitating, spherical accretion onto a point mass. In his solution the gas is at rest at infinity, with a finite sound speed c_∞. As the gas falls toward the center, it passes through a sonic point (for ratio of specific heats $\gamma < 5/3$) with radius r_c, where $-v = c =$ local sound speed. Outside r_c the flow is very different from that considered here, but for $r \ll r_c$ the flow is highly supersonic, and the solution, suitably nondimensionalized, matches equations (2.14), (2.16), and (2.24).

III. SHOCKED ACCRETION OF A COLLISIONAL GAS

If there is no central black hole, infalling fluid elements either pass through the origin and through other infalling elements (if the fluid is collisionless) or are decelerated by passage through a shock and by postshock pressure gradients so that they come to rest at the center (if the fluid is collisional). The latter case is considered in this section. It is somewhat simpler than the former case, discussed in § IV, because shell-crossing does not occur.

It is useful here to continue the analogy with Bondi (1952) accretion, as discussed at the end of § II. To compare it with shocked infall solutions, we must consider the generalization of the Bondi solution to include a shock. McCrea (1956) showed that a standing shock may be inserted in the Bondi flow interior to the sonic point. For $1 < \gamma < 3/2$, satisfactory "settling" solutions exist, with $v = 0$ at $r = 0$; however, no steady settling solutions exist for $\gamma \geq 3/2$. This point was not mentioned by McCrea, although it follows from his analysis and the form of the Bondi solutions inside the sonic radius. The physical explanation is that for too stiff an equation of state the shock propagates outward. In actual accretion onto, e.g., a white dwarf, radiation is important, and steady solutions with standing shocks then exist (Hoshi 1973; Aizu 1973; Fabian, Pringle, and Rees 1976), although they may not be stable (Chevalier and Imamura 1982).

Here we assume that the postshock flow is adiabatic with a ratio of specific heats γ (i.e., radiation is neglected), but the resulting shocked infall solutions are very different from the solutions found by McCrea. Since we are considering cosmological infall, the preshock boundary conditions are those given in § II for a pressureless gas. The shock is therefore strong, whereas McCrea's shocks have finite Mach number. Semianalytic solutions exist here for all $\gamma > 4/3$ and are self-similar rather than steady. Also, the gas is self-gravitating, and there is no longer a central black hole, so the mass flux vanishes at the origin. Similarity solutions exist, but are not given here, for accretion rates $\dot{m}$ intermediate between 0 and the maximum rate $\dot{m}_{\text{bh}}$ (eq. [2.25]) for cold accretion; for $0 < \dot{m} < \dot{m}_{\text{bh}}$ shocks form and propagate with the same expansion law as that given below (eq. [3.1]), but with a smaller numerical coefficient because the pressure driving the expansion is less (see discussion at the end of this section).

Changing the central boundary conditions from free fall to $v = 0$ does not add any new dimensional parameters, so the solutions for shocked accretion are self-similar, like those of § II for cold accretion, with the appropriate scale length given by the turnaround radius equation (2.7). The shock occurs at fixed $\lambda = \lambda_s \equiv r_s / r_{\text{ta}}$ and thus propagates according to

$$r_s(t) = \lambda_s r_{\text{ta}}(t) \propto t^{8/9}. \tag{3.1}$$

The nondimensional shock radius λ_s will be determined below.

The analysis leading to the collisional infall similarity solutions is similar to that given in Paper I for voids and by Bertschinger (1983) for cosmological blast waves. The fluid variables are nondimensionalized according to (cf. eqs. [2.13], [2.15], and [2.21])

$$v(r,t) = \frac{r_{\text{ta}}}{t} V(\lambda), \qquad \rho(r,t) = \rho_{\text{H}} D(\lambda),$$

$$p(r,t) = \rho_{\text{H}} \left(\frac{r_{\text{ta}}}{t}\right)^2 P(\lambda), \qquad m(r,t) = \frac{4}{3}\pi \rho_{\text{H}} r_{\text{ta}}^3 M(\lambda). \tag{3.2}$$

The radius is nondimensionalized as in equation (2.9). (Note, however, that $\lambda = \lambda[\theta]$ given in eq. [2.9] applies only for $\lambda > \lambda_s$.)

The equations describing the motion of a collisional fluid are

$$\frac{d\rho}{dt} \equiv \left(\frac{\partial}{\partial t} + v\frac{\partial}{\partial r}\right)\rho = -\rho \frac{1}{r^2}\frac{\partial}{\partial r}(r^2 v), \tag{3.3a}$$

$$\frac{dv}{dt} = -\frac{1}{\rho}\frac{\partial p}{\partial r} - \frac{Gm}{r^2}, \tag{3.3b}$$

$$\frac{d}{dt}(p\rho^{-\gamma}) = 0, \tag{3.3c}$$

$$\frac{\partial m}{\partial r} = 4\pi r^2 \rho. \tag{3.3d}$$

These are respectively the continuity, Euler, adiabatic, and mass equations and are valid for the postshock flow neglecting radiation, heat conduction, magnetic fields, nonspherical symmetry, etc. The fluid equations are nondimensionalized using equations (2.9) and (3.2) to give (cf. eqs. [2.41] of Paper I)

$$\left(V - \frac{8}{9}\lambda\right)D' + DV' + \frac{2DV}{\lambda} - 2D = 0, \tag{3.4a}$$

$$\left(V - \frac{8}{9}\lambda\right)V' - \frac{1}{9}V = -\frac{P'}{D} - \frac{2}{9}\frac{M}{\lambda^2}, \tag{3.4b}$$

$$\left(V - \frac{8}{9}\lambda\right)\left(\frac{P'}{P} - \gamma\frac{D'}{D}\right) = \frac{20}{9} - 2\gamma, \tag{3.4c}$$

$$M' = 3\lambda^2 D, \tag{3.4d}$$

where primes denote derivatives with respect to λ. Self-similarity reduces the partial differential fluid equations (3.3) to ordinary differential equations whose integration is comparatively straightforward.

The preshock boundary conditions (denoted by subscript 1) are obtained from equations (2.13), (2.15), and (2.21) for pressureless infall:

$$V_1 = \frac{\lambda_s \sin\theta_s(\theta_s - \sin\theta_s)}{(1-\cos\theta_s)^2}, \qquad D_1 = \frac{d_s^2 \beta_s^{-3}}{1+3\chi_s},$$

$$P_1 = 0, \qquad M_1 = \lambda_s^3 d_s^2 \beta_s^{-3}, \tag{3.5}$$

where θ_s, β_s, d_s, and χ_s are given in terms of the unknown λ_s in equations (2.5), (2.6), (2.9), and (2.21). The nondimensional shock jump conditions,

$$V_2 = \frac{8}{9}\lambda_s + \frac{\gamma-1}{\gamma+1}\left(V_1 - \frac{8}{9}\lambda_s\right), \qquad D_2 = \frac{\gamma+1}{\gamma-1}D_1,$$

$$P_2 = \frac{2}{\gamma+1}D_1\left(V_1 - \frac{8}{9}\lambda_s\right)^2, \qquad M_2 = M_1, \tag{3.6}$$

then give the starting values for numerical integration of equations (3.4) inward from $\lambda = \lambda_s$. The eigenvalue λ_s is determined by requiring the solutions to satisfy the inner boundary conditions

$$V = M = 0, \qquad \lambda = 0. \tag{3.7}$$

Another constraint on the solution comes from energy conservation: the total postshock energy must equal the total energy given in equation (2.10) for the initial shell being shocked, since the energy interior to a shell is constant until it is shocked. Using equations (2.2), (2.5), (2.9), (2.10), and (3.2), energy conservation gives, when nondimensionalized,

$$t + u + w = E(\lambda_s) \equiv -\frac{1}{3}\left(\frac{3\pi}{4}\right)^{40/9} d_s^{-4/9}, \tag{3.8}$$

where t, u, and w are the nondimensional mean kinetic, thermal, and gravitational energies within the shock:

$$t \equiv \int_0^{M_2} \frac{1}{2} V^2\, dM, \qquad u \equiv \int_0^{M_2} \frac{P/D}{\gamma-1}\, dM,$$

$$w \equiv -\frac{2}{9} \int_0^{M_2} \frac{M}{\lambda}\, dM; \tag{3.9}$$

M is used as the variable of integration (cf. eq. [3.4d]) for consistency with § IV. It is not clear mathematically that equations (3.7) and (3.8) can all be satisfied with the same value of λ_s, although physically they must if the solutions are to be sensible.

The system of nondimensional fluid equations (3.4) with boundary conditions (3.6) has analytic integrals of the motion which provide a useful check of the numerical integrations. In addition to the mass integral (2.27), which may be verified here by substituting into equations (3.4a), (3.4d), and (3.6), there is an entropy integral (Bertschinger 1983)

$$PD^{-\gamma}M^{\zeta} = P_2 D_2^{-\gamma} M_2^{\zeta} = \text{const}, \qquad \zeta \equiv \frac{10}{3} - 3\gamma, \tag{3.10}$$

which may be verified by substituting into equations (3.4a), (3.4c), and (3.4d).

A final global check of the integrations is provided by the virial theorem, which, when applied to the shock-enclosed volume and nondimensionalized, becomes

$$\frac{143}{81} \int_0^{M_2} \lambda^2\, dM = 2t + 3(\gamma-1)u + w - 3\lambda_s^3 D_2 \left(V_2 - \frac{8}{9}\lambda_s\right)\left(V_2 + \frac{13}{18}\lambda_s\right). \tag{3.11}$$

The first term in equation (3.11) is the nondimensionalized $\frac{1}{2} d^2 I/dt^2$, where I is the moment of inertia, and the last term is due to the flux of inertia through the bounding surface $\lambda = \lambda_s$. In the absence of these terms equation (3.11) gives the usual result $2t + 3(\gamma-1)u + w = 0$ for steady motion. Since the motion here is self-similar, not steady, all the terms of equation (3.11) are nonzero and must be included.

Since the shocked infall solutions are singular at the origin, it is necessary to determine and factor out the asymptotic behavior before equations (3.4) can be integrated numerically all the way to $\lambda = 0$. Using the inner boundary conditions (3.7), analysis of equations (3.4) shows that the fluid variables may be written, for $\gamma > 4/3$,

$$D = \lambda^{-9/4} \tilde{D}(\lambda), \qquad P = \lambda^{-5/2} \tilde{P}(\lambda), \qquad M = \lambda^{3/4} \tilde{M}(\lambda), \tag{3.12}$$

where $\tilde{D}$, $\tilde{P}$, and $\tilde{M}$ are finite at $\lambda = 0$. The case $\gamma = 4/3$ will be discussed separately. The dependence of V on λ near $\lambda = 0$ depends on γ and is determined numerically below.

The density profile in equation (3.12), $\rho \propto r^{-2.25}$ near $r = 0$, was first derived by Gott (1975), by assuming that after they turn around, mass shells remain (on average) at a constant fraction of their turnaround radius. As will be shown below, this is exactly what happens in the $\gamma > 4/3$ collisional solutions after a fluid element crosses the shock.

Equations (3.4) with initial conditions (3.6) were integrated after changing the dependent variables (eqs. [3.12]) with 1000 points using a fifth-order and sixth-order Runge-Kutta ordinary differential equation solver for $\gamma = 5/3$, $3/2$, $7/5$, and $4/3$. For each value of γ a unique value of λ_s was found to satisfy the inner boundary conditions (3.7). At each point $\lambda > 0$ in the integrations, the integrals of motion (2.27) and (3.10) were checked and had relative errors less than 6×10^{-9}. The solutions for $\gamma = 5/3$ and $4/3$ are shown in Figures 2 and 3, and are tabulated in Tables 1 and 2. The quantities D, P, and M have been plotted on logarithmic axes to show the power-law behavior near $\lambda = 0$. The solutions have a number of interesting features. First, the velocity decrease across the shock is very large: $V_2/V_1 = 10.4$ for $\gamma = 5/3$, although the jump in the frame of the outward-moving shock is less, given by equation (3.6) (a factor of 4 for $\gamma = 5/3$). The large velocity decrease implies large postshock pressures and temperatures; together these imply that the postshock kinetic energy is much less than the thermal and gravitational energies. Next, the shock occurs at a relatively small fraction of the turnaround radius, with the shock radius decreasing as the equation of state becomes softer, allowing the gas to be compressed more. Because the fluid falls back much of the way before being shocked, the preshock density is substantially higher than the unperturbed density $\rho_{\rm H}$. The mean postshock density, $M_1 \lambda_s^{-3}$ in units of $\rho_{\rm H}$, is very high (97.2 for $\gamma = 5/3$, increasing to 2.95×10^3 for $\gamma = 4/3$). Near the origin the numerical solutions give $V \propto \lambda^k$, with $k = 2$, 1.7, and 1.4 for $\gamma = 5/3$, $3/2$, and $7/5$, respectively. For $\gamma = 4/3$, $k \approx 1.3$, but a single power law does not fit the velocity well, which is numerically not well determined close to $\lambda = 0$.

Although it is unnecessary to calculate the trajectory of a fluid particle to obtain the collisional similarity solutions, the trajectory is of interest because it increases our physical understanding of the solutions. The trajectories for $\gamma = 5/3$, $3/2$, $7/5$ and $4/3$ were calculated using equation (5.4) (see § V) and are plotted in Figure 4. Instead of graphing the trajectory as $\lambda(\xi)$, where $\lambda = (r/r'_{\rm ta})(t/t_{\rm ta})^{-8/9}$ and $\xi = \ln(t/t_{\rm ta})$, it is more useful to examine $r/r'_{\rm ta}$ vs. $t/t_{\rm ta}$, where $t_{\rm ta}$ and $r'_{\rm ta} \equiv r_{\rm ta}(t_{\rm ta})$ are the constant turnaround time and radius of a particular mass shell. (By contrast, $\lambda = r/r_{\rm ta}[t]$ is nondimensionalized using the current, time-varying turnaround radius.) The trajectories of Figure 4 are valid for all particles, on condition that the units are provided by the turnaround time and radius of the particle under consideration. Before being shocked, a collisional fluid particle follows the trajectory for cold accretion onto a black hole (*dashed curve*). The shock causes the velocity to change discontinuously and hence occurs where the slope of the trajectory changes. We see that after it is shocked, a collisional fluid particle settles to a constant fraction $r_\infty/r'_{\rm ta}$ of its turnaround radius. This shows why the derivation by Gott (1975) of the mass and density exponents of equation (3.12) is correct. For $\gamma = 5/3$, $r_\infty/r'_{\rm ta} = 0.4326$. For $\gamma = 4/3$, it appears that $r/r'_{\rm ta}$

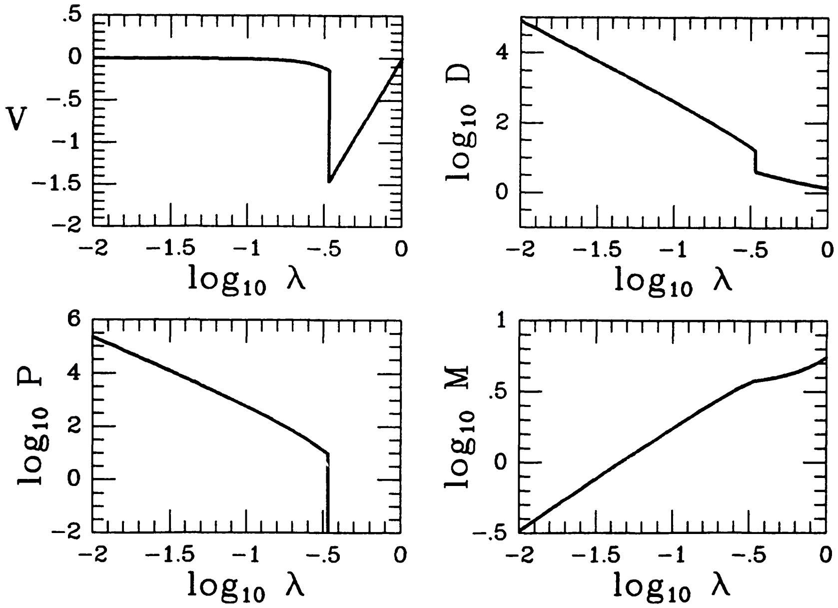

FIG. 2.—Self-similar accretion of a $\gamma = 5/3$ collisional gas. The velocity V, density D, pressure P, and mass M are plotted vs. radius λ, with units given by eqs. (2.9) and (3.2). The preshock solution is given in Fig. 1.

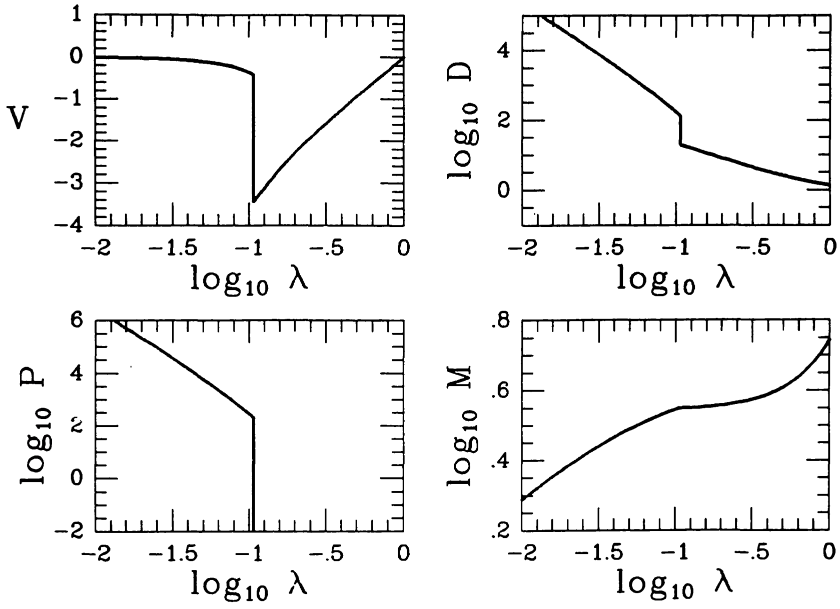

FIG. 3.—Same as Fig. 2, except $\gamma = 4/3$

$\rightarrow 0$ as $t/t_{\text{ta}} \rightarrow \infty$, explaining why equation (3.12) is not valid for $\gamma = 4/3$ (see also below). The same should be true for $\gamma < 4/3$, since a softer equation of state diminishes further the role of pressure forces, although these solutions have not been calculated because of numerical difficulties. These results imply that if cooling occurs, leading to an effective $\gamma < 4/3$, central collapse must occur, and they suggest that spherical collapse will lead to a black hole unless other processes halt the collapse at $r > 0$. The physical origin of this collapse will be discussed further in § V.

Several of the constants of the similarity solutions are given in Table 3. Note that the shock occurs at a fraction λ_s of the current turnaround radius, less than the fraction r_s/r'_{ta} of the turnaround radius of the shell currently being shocked. The two differ because a particle is not shocked until somewhat after it has turned around (see Fig. 4); in the meantime the turnaround radius has moved outward. The parameters $\tilde{D}(0)$, $\tilde{P}(0)$, and $\tilde{M}(0)$ (cf. eq. [3.12]), giving the leading behavior of the solution (for $\gamma > 4/3$) near $\lambda = 0$, were calculated by least-squares fitting $\tilde{D}$, $\tilde{P}$, and $\tilde{M}$ to a power series for a

TABLE 1

COSMOLOGICAL SELF-SIMILAR ACCRETION FOR $\Omega = 1$ COLLISIONAL GAS, $\gamma = 5/3$

λ	V	D	P	M
0	0	∞	∞	0
0.016949......	−1.78891(−4)	2.45907(+4)	6.12868(+4)	0.484591
0.033898......	−7.32196(−4)	5.06185(+3)	1.03074(+4)	0.807802
0.050846......	−1.68684(−3)	1.98945(+3)	3.55489(+3)	1.08515
0.067795......	−3.07273(−3)	1.01861(+3)	1.64403(+3)	1.33433
0.084744......	−4.92334(−3)	6.02683(+2)	8.92403(+2)	1.56305
0.101693......	−7.27634(−3)	3.90646(+2)	5.35790(+2)	1.77558
0.118642......	−1.01745(−2)	2.69593(+2)	3.44696(+2)	1.97460
0.135591......	−1.36665(−2)	1.94741(+2)	2.33154(+2)	2.16199
0.152539......	−1.78088(−2)	1.45628(+2)	1.63784(+2)	2.33908
0.169488......	−2.26669(−2)	1.11888(+2)	1.18482(+2)	2.50687
0.186437......	−2.83181(−2)	8.78453(+1)	8.77267(+1)	2.66616
0.203386......	−3.48545(−2)	7.01919(+1)	6.61797(+1)	2.81756
0.220335......	−4.23874(−2)	5.69023(+1)	5.06849(+1)	2.96158
0.237283......	−5.10541(−2)	4.66834(+1)	3.92951(+1)	3.09861
0.254232......	−6.10267(−2)	3.86804(+1)	3.07644(+1)	3.22897
0.271181......	−7.25262(−2)	3.23109(+1)	2.42704(+1)	3.35292
0.288130......	−8.58450(−2)	2.71673(+1)	1.92555(+1)	3.47066
0.305079......	−1.01383(−1)	2.29576(+1)	1.53322(+1)	3.58231
0.322028......	−1.19715(−1)	1.94671(+1)	1.22256(+1)	3.68796
0.338976$^-$ ...	−1.41715(−1)	1.65341(+1)	9.73563	3.78759
0.338976$^+$ ...	−1.47080	4.13353	0	3.78759

NOTE.—Units are given in eqs. (2.9) and (3.2).

TABLE 2

COSMOLOGICAL SELF-SIMILAR ACCRETION FOR $\Omega = 1$ COLLISIONAL GAS, $\gamma = 4/3$

λ	V	D	P	M
0	0	∞	∞	0
0.005316	−4.55429(−3)	1.30479(+6)	2.44794(+7)	1.54011
0.010633	−1.13373(−2)	1.87125(+5)	2.17207(+6)	1.97915
0.015949	−1.96386(−2)	5.83979(+4)	5.02406(+5)	2.26058
0.021266	−2.93057(−2)	2.51503(+4)	1.73221(+5)	2.46745
0.026582	−4.02873(−2)	1.29399(+4)	7.45155(+4)	2.62991
0.031899	−5.25763(−2)	7.45503(+3)	3.69143(+4)	2.76264
0.037215	−6.61916(−2)	4.64524(+3)	2.01705(+4)	2.87402
0.042532	−8.11715(−2)	3.06581(+3)	1.18451(+4)	2.96926
0.047848	−9.75705(−2)	2.11436(+3)	7.35074(+3)	3.05189
0.053165	−1.15459(−1)	1.50963(+3)	4.76484(+3)	3.12437
0.058481	−1.34927(−1)	1.10844(+3)	3.19929(+3)	3.18852
0.063798	−1.56081(−1)	8.32787(+2)	2.21121(+3)	3.24569
0.069114	−1.79057(−1)	6.37773(+2)	1.56558(+3)	3.29695
0.074431	−2.04020(−1)	4.96343(+2)	1.13116(+3)	3.34312
0.079747	−2.31177(−1)	3.91562(+2)	8.31395(+2)	3.38486
0.085064	−2.60791(−1)	3.12472(+2)	6.19975(+2)	3.42271
0.090380	−2.93203(−1)	2.51778(+2)	4.67964(+2)	3.45712
0.095697	−3.28865(−1)	2.04503(+2)	3.56778(+2)	3.48843
0.101013	−3.68397(−1)	1.67169(+2)	2.74177(+2)	3.51695
0.106329$^-$ ...	−4.12683(−1)	1.37298(+2)	2.11919(+2)	3.54291
0.106329$^+$ ...	−3.45587	1.96140(+1)	0	3.54291

NOTE.—Units are given in eqs. (2.9) and (3.2).

few points at $\lambda > 0$ and extrapolating back to $\lambda = 0$, with the integrals (2.27) and (3.10) providing a check at $\lambda = 0$. The energy integrals of equation (3.9) were calculated using cubic splines quadrature. Global integral checks of the quadratures, given by equations (3.8) and (3.11), were satisfied to better than 1% for $\gamma = 7/5$ and to 2×10^{-8} for $\gamma = 5/3$. The solutions become increasingly ill-behaved near $\lambda = 0$ with decreasing γ; it was not possible to accurately determine several of the parameters for $\gamma = 4/3$, although the good agreement of the local integrals of motion implies that the $\gamma = 4/3$ solution is accurate for $\lambda > 10^{-3}$.

Although $\gamma = 5/3$ is the only case occurring in practice for an adiabatic gas, the $\gamma = 4/3$ solution deserves more attention because of its interesting mathematical and physical properties. Also, it is desirable to understand the behavior of the adiabatic solutions for small γ since radiative cooling is similar in its effects to decreasing γ. For $\gamma = 4/3$, the integrals (2.27) and (3.10) imply that near $\lambda = 0$

$$D \sim \lambda^{c_D}, \qquad P \sim \lambda^{c_P}, \qquad M \sim \lambda^{c_M},$$

with $c_P = 2c_D + 2$ and $c_M = c_D + 3$. The Euler equation (4b) shows that inertial forces are unimportant at the origin, where pressure forces balance gravity (a kind of time-dependent hydrostatic equilibrium), but it does not provide an additional condition between c_D, c_P, and c_M for the degenerate case $\gamma = 4/3$. It is not clear that c_D can be determined analytically from the equations of motion, so the numerical solutions were examined. They give $c_D \approx -2.6$, $c_P \approx -3.2$, and $c_M \approx 0.4$. The density and pressure fall off more steeply with λ than in equation (3.12) (also cf. Figs. 2 and 3), and the mass converges to zero more slowly as $\lambda \to 0$. The striking implication of these results is, however, that the thermal and gravitational energies diverge as $\lambda^{-0.2}$ at the origin. At first this seems nonsensical, but only the sum of u and w, the total energy (minus the small kinetic energy term t), need be finite; since the constraints on c_D, c_P, and c_M assure that u and w diverge at the same rate, it is reasonable that there may be cancellation, leaving a finite remainder as $\lambda \to 0$. Nevertheless this result is anti-intuitive, and no explanation has been found, although Figure 4 suggests that the $\gamma = 4/3$ solution should behave in an unusual fashion as $\lambda \to 0$, because the fluid particles do not settle at a finite fraction of their turnaround radii but rather fall all the way back to the center.

The shock position λ_s was determined by requiring the inner boundary conditions (3.7) to be satisfied. Different values of λ_s correspond to different central boundary conditions, which may have physical significance. The qualitative effects of varying λ_s are discussed now, although detailed numerical solutions are not given.

First, decreasing λ_s causes the mass M to be positive at the origin. This corresponds for $\lambda_s > 0$ to placing at $r = 0$ a black hole of mass less than the maximum value given in equation (2.16). (In the limit $\lambda_s \to 0$ the complete solution of § II is recovered.) Infalling fluid elements are first shocked and fall in subsonically but then pass through a sonic point. Interior to this the solution approaches the asymptotic free-fall Bondi form given by equations (2.14), (2.16), and (2.24). Any accretion rate between zero (the collisional case with no black hole) and the maximum rate given by equation (2.26) can be achieved by varying λ_s. The question of which rate occurs physically may depend on the stability properties of the solutions, which cannot be determined from the self-similar analysis given here. Intuitively we expect radiative cooling to cause further gravi-

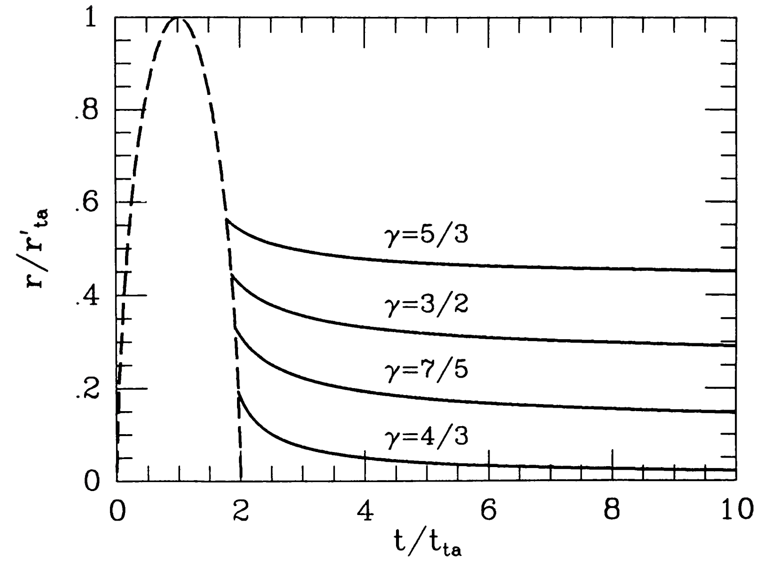

FIG. 4.—Trajectories of a collisional fluid particle (*solid curves*) for several specific heat ratios γ in the shocked-accretion similarity solution. The turnaround time and radius of the particle are $t_{\rm ta}$ and $r'_{\rm ta}$; the trajectories are valid for all particles when so scaled. Shocks occur where the trajectories break away from the trajectory for cold accretion onto a black hole (*dashed curve*). The collisional trajectories approach constant values $r_\infty/r'_{\rm ta}$ as $t/t_{\rm ta} \rightarrow \infty$.

TABLE 3

CONSTANTS OF THE $\Omega = 1$ COLLISIONAL COSMOLOGICAL SELF-SIMILAR ACCRETION SOLUTIONS

Parameter	$\gamma = 5/3$	$\gamma = 3/2$	$\gamma = 7/5$	$\gamma = 4/3$[a]
λ_s	0.338976	0.257297	0.185732	0.106329
$r_s/r'_{\rm ta}$	0.564393	0.444877	0.330095	0.193525
θ_s	4.58324	4.82286	5.05910	5.37218
V_1	−1.47080	−1.87897	−2.40451	−3.45587
D_1	4.13353	5.86384	9.04185	19.6140
M_1	3.78759	3.68187	3.60668	3.54291
$\tilde{D}(0)$	2.60173	3.85606	8.1727	...
$\tilde{P}(0)$	2.40676	5.28683	23.749	...
$\tilde{M}(0)$......	10.4069	15.4243	32.692	...
t/E[b]......	4.13433(−4)	7.06(−4)	1.10(−3)	...
u/E	1.15343	2.287	5.55	...
w/E	−2.15384	−3.288	−6.55	...
$r_\infty/r'_{\rm ta}$	0.4326	0.257	0.10	< 5.(−3)

[a] Omitted values are poorly determined.
[b] Here $E \equiv |t + u + w|$.

tational collapse in the center, perhaps leading to the formation of a black hole, thereby decreasing λ_s. It is also possible if cooling occurs that the solutions are thermally unstable to oscillations of the shock front (cf. Chevalier and Imamura 1982).

If λ_s is increased above the critical values found above, the solutions do not extend all the way to $\lambda = 0$; rather, $M = 0$ at $\lambda = \lambda_0 > 0$, $V = \frac{8}{9}\lambda_0$. The infalling matter passes through a turning point $V = 0$ at some λ such that $\lambda_0 < \lambda < 1$. The density and pressure of the accreted matter are still singular at $M = 0$. These solutions are less plausible physically but may occur if a central wind or explosion ejects matter, with the ejecta separated from the infalling matter by a contact discontinuity at $\lambda = \lambda_0$.

IV. COLLISIONLESS INFALL

The similarity solution for secondary infall of a collisionless gas differs from the cases discussed in §§ II and III in that infalling fluid particles are not stopped at the center by a black hole or boundary conditions, so shell-crossing occurs. To treat this case it is therefore necessary to adopt a Lagrangian viewpoint, following each particle separately. Fortunately it is not necessary to calculate the orbits of many different particles, as is done in an N-body code, since, as will be shown below, the trajectories are all identical when suitably scaled. The solution technique is the same as that used in Paper I to give the motion of a collisionless fluid outside an uncompensated hole.

We consider the motion of a particle which turns around at cosmic time $t_{\rm ta}$, with $t_{\rm ta} \gg t_{\rm ita}$ (eq. [1.3]), so that the initial collapse has occurred long before $t_{\rm ta}$. At $t_{\rm ta}$ the particle is at its maximum radius, $r'_{\rm ta} \equiv r_{\rm ta}(t_{\rm ta})$. In order to derive some results depending on self-similarity the particle trajectory $r = r(t)$ is written first in the nondimensional form $\lambda = \lambda(\xi)$, where $\xi \equiv \ln(t/t_{\rm ta})$ and $\lambda \equiv r/r_{\rm ta}(t)$ (eq. [2.9]). Notice that r is nondimensionalized here in terms of the current turnaround radius $r_{\rm ta}(t)$, not the turnaround radius $r'_{\rm ta}$ of the particle. The unscaled (in time) radius $r/r'_{\rm ta} = \lambda e^{(8/9)\xi}$ will be recovered below with very interesting results.

The dimensional trajectory obeys Newton's law (2.1), where now $m = m(r, t)$ is the mass interior to $r(t)$, and is not constant for the Lagrangian particle, because of shell-crossing. At first this complication seems to make the problem intractable without an N-body calculation. Because of the self-similarity, however, much simplification occurs when the problem is recast in nondimensional terms. The key is that, at time $t \gg t_{\rm ita}$, there are a unique length scale $r_{\rm ta}(t)$ and density scale $\rho_{\rm H}(t)$. Thus the mass may be written as in equation (3.2), with the nondimensional M depending only on λ, not on ξ. The emphasis placed here and previously on these standard arguments from dimensional analysis is not exaggerated in view of their power, as we will see shortly.

When the mass and radius are nondimensionalized as described above, the equation of motion (2.1) becomes

$$\frac{d^2\lambda}{d\xi^2}+\frac{7}{9}\frac{d\lambda}{d\xi}-\frac{8}{81}\lambda=-\frac{2}{9}\frac{M(\lambda)}{\lambda^2}, \qquad (4.1)$$

with initial conditions

$$\lambda=1, \quad \frac{d\lambda}{d\xi}=-\frac{8}{9} \quad \text{at} \quad \xi=0. \qquad (4.2)$$

Notice that nondimensionalizing and changing the independent variable from t to $\ln t$ has eliminated the explicit time dependence (ξ-dependence), although it has introduced two additional terms into the equation of motion. The velocity-dependent term produces an effective time-dependent potential. This is to be expected since $m=m(r,t)$ and the gravitational potential *is* time dependent. Because of this fact the energy of a particle is not constant along its trajectory, so phase-mixing and violent relaxation (Lynden-Bell 1967) will occur. The beauty of the self-similarity is that it reduces this difficult time-dependent problem, with potential determined by $m=m(r,t)$, to one where the potential depends on a function of a single variable, $M=M(\lambda)$, which is much easier to solve. This does *not* mean that equation (4.1) neglects the other particles or holds them fixed in position in describing the motion of one particle. The motion *of all particles simultaneously*, with all possible phases in their orbits, is given by the solution of equation (4.1).

The most important feature of equation (4.1) is its translation symmetry: since ξ does not appear explicitly (only $d\xi$ does), it follows that if $\lambda=\lambda(\xi)$ is a solution, then so is $\lambda=\lambda(\xi+a)$, for arbitrary a. This fact makes it unnecessary to do detailed time-dependent calculations with many particles, since a single integration of equation (4.1) with initial conditions (4.2) suffices to give the solution for *all* particles after they first turn around. This is a general feature of similarity solutions: the particle trajectories all look the same when scaled appropriately in time (i.e., translated in ξ). Notice that a Lagrangian particle may be labeled by its turnaround time $t_{\rm ta}$ or radius $r'_{\rm ta}$, or by its value of $\xi=\ln(t/t_{\rm ta})$ at some time t. Thus ξ may be thought of either as giving the time t for a single particle, with fixed $t_{\rm ta}$, or as a Lagrangian variable distinguishing different particles at the same time t.

There is one important task to be completed before the collisionless infall similarity solution can be given. The nondimensional mass distribution $M(\lambda)$ must be specified before equation (4.1) can be integrated. It was shown in Paper I that M is completely determined by the trajectory $\lambda(\xi)$. Physically this is because $\lambda(\xi)$ gives a complete phase-space description of the self-similar motion since, as was shown above, $\lambda(\xi)$ gives the trajectory of every particle. One way of obtaining $M(\lambda)$, used in N-body codes, is to take many different particles and to advance each along its trajectory; then to bin the particles in radius and add up the number of particles interior to varying radii λ. This is tedious, and especially inaccurate near $\lambda=0$, where $M\to 0$. Fortunately there is an elegant analytic solution, derived in Paper I:

$$M(\lambda)=M_{\rm ta}\sum_i(-1)^{i-1}\exp\left[-(2/3)\xi_i\right], \qquad (4.3)$$

where $M_{\rm ta}$ is a normalization constant given by equation (2.23). The sum is over points ξ_i for which the trajectory has the value λ; i.e., ξ_i is the value of ξ at the ith point where $\lambda=\lambda(\xi)$. The derivation rests on the result, shown above, that ξ may be used as a Lagrangian variable distinguishing different mass elements. Particles with $\xi<\xi_1$ have not yet fallen through the center and are still exterior to λ; those with $\xi_1<\xi<\xi_2$ lie interior to λ; those with $\xi_2<\xi<\xi_3$ have fallen through once and have passed back beyond λ; and so on. The sum adds (for i odd) the mass of particles interior to λ and subtracts (for i even) the mass of particles which are exterior to λ, having crossed λ moving outward; thus shell-crossing is correctly accounted for. The exponential occurs because, while the dimensional mass dm of a Lagrangian fluid element is constant, it becomes a smaller and smaller part of the total mass, which increases as $t^{2/3}$. Thus the *nondimensional* mass of a Lagrangian particle decreases as $e^{-(2/3)\xi}$. There are a finite number of terms in the series for $\lambda>0$, with the number increasing as λ decreases. Full details of the derivation of equation (4.3) are given in Paper I.

While equation (4.3) gives the self-similar mass distribution for the exact self-similar trajectory $\lambda(\xi)$, M must be known before equation (4.1) can be integrated to obtain $\lambda(\xi)$. An iterative method of solution is therefore used. A guess is first made for the mass distribution; e.g., $M(\lambda)=M_{\rm ta}\lambda^{3/4}$ for $\lambda\leq 1$. Equation (4.1) may then be integrated to find $\lambda(\xi)$; equation (4.3) gives a new approximation to $M(\lambda)$; and so on, until a self-consistent solution is found.

The method of solution outlined above is straightforward, but there is one computational difficulty which had to be solved, viz., the singular behavior of the solutions at $\lambda=0$. The physical origin of the problem is that after an infalling particle reaches the center, it moves back again to increasing λ, with $d\lambda/d\xi$ changing discontinuously from negative to positive values at $\lambda=0$; furthermore, in the self-similar solution the velocity becomes infinite at the origin. This discontinuity is difficult to handle numerically. Several remedies were tried, including reflecting the trajectory close to the origin and taking a sufficiently large time step so as to pass through the center without noticing it. After some experimentation, the best solution was found to be to give the particle a small amount of angular momentum so that it avoids $\lambda=0$ altogether. If the angular momentum vectors are distributed uniformly over a sphere, this adds a term $+J^2/\lambda^3$ to the right-hand side of equation (4.1), producing a strong repulsive force for $\lambda \ll J^{2/3}$. A value of $J^2=10^{-9}$ proved sufficient; with this small value the solutions are essentially unaffected by the angular momentum at the radii tabulated and graphed below.

Equation (4.1) was integrated with 2000 points evenly spaced in ξ, $0\leq\xi\leq 3\ln 10$, corresponding to a span of 1000 Hubble times after the initial collapse at $t_{\rm ita}$. Because a finite integration cannot account for all particles which have turned around

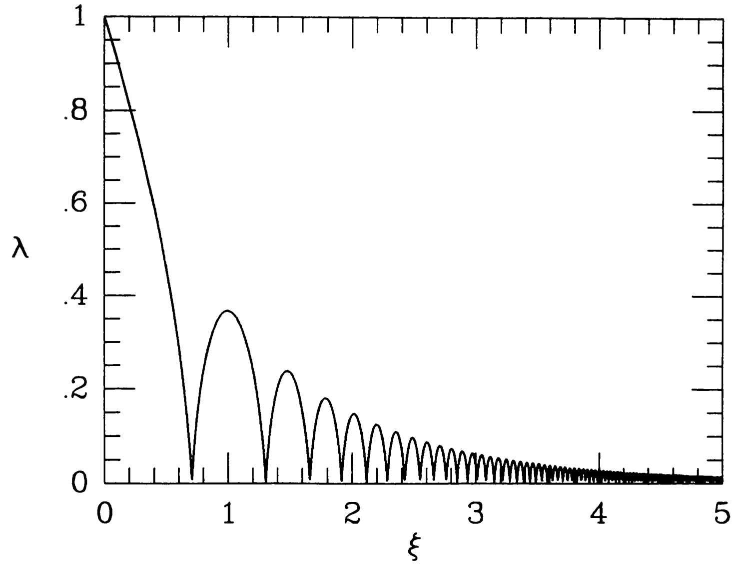

FIG. 5.—Nondimensional trajectory $\lambda(\xi)$ for a fluid particle in the collisionless infall similarity solution. The dimensional radius is $r = \lambda r_{\rm ta}(t)$, where $r_{\rm ta} \propto t^{8/9}$ is the current, time-varying turnaround radius; the abscissa is $\xi = \ln(t/t_{\rm ta})$. The particle reaches its maximum radius at $t = t_{\rm ta}$, $r = r_{\rm ta}(t_{\rm ta})$, or $\xi = 0$, $\lambda = 1$. Note the many oscillations as $\xi \to \infty$; each is an orbit passing through the center $\lambda = 0$.

(i.e., the exact self-similar solution has particles turning around beginning at $t_{\rm ita} = 0$, while a nonzero starting time must be used for numerical integrations), this time span resulted in mass and energy errors of several percent, but using more points proved too costly. A modification of the integration scheme which gave greater accuracy at less expense will be discussed below. The mass was obtained from equation (4.3), using cubic splines interpolation to obtain the intersection points ξ_i. About 10 iterations were calculated, by which time $\lambda(\xi)$ was changing by less than 1% per iteration. The nondimensional trajectory is shown in Figure 5. When the particle passes through the center, it moves immediately again to $\lambda > 0$, explaining the many reflections of the trajectory at $\lambda = 0$. Figure 5 shows that as the turnaround radius continues to increase, the maximum radius of the particle in its orbit becomes relatively smaller. This does not necessarily imply that the absolute radius of the orbit decreases; this point is important and will be discussed below. Since the abscissa is a logarithmic time scale and, as we will see, the orbit period approaches a constant after many orbits, the orbits become increasingly compressed for large ξ.

The particular nondimensionalization of the trajectory adopted in Figure 5 is useful because $\lambda(\xi)$ may be interpreted as giving either the nondimensional trajectory for a single particle or the radius of different particles at a fixed time, with ξ being a Lagrangian variable. This dual interpretation shows how the solution gives the simultaneous position and motion of every particle. Position and velocity information is best expressed in the phase-space diagram, Figure 6, which graphs $d\lambda/d\xi$ versus $\log \lambda$. The dimensional velocity of a particle is obtained (using the definition of λ in eq. [2.9]) from

$$v = \frac{r_{\rm ta}(t)}{t} V(\xi), \qquad V(\xi) = \frac{d\lambda}{d\xi} + \frac{8}{9}\lambda . \tag{4.4}$$

Like Figure 5, Figure 6 has two interpretations. The first is that of a fixed particle moving along the phase curve, beginning at $\lambda = 1, d\lambda/d\xi = -8/9$. It moves to the left along the first branch until $\lambda = 0$, and then it reappears at the upper left-hand corner of the figure after crossing through the center. The particle traces successive branches on successive orbits. This interpretation must be applied carefully because λ is not the true radius of the particle; e.g., even if it remains at fixed r, the particle will follow a path $d\lambda/d\xi = -(\frac{8}{9})\lambda$ (cf. eq. [4.4]). The second interpretation is clearer and more useful: Figure 6 shows the range of particle positions and velocities present at a fixed time. It illustrates the phase-mixing that occurs during collapse and subsequent infall: every point of the phase curve is occupied by some particle in the similarity solution. It should be emphasized that two-body collisions have not contributed at all to the phase-mixing, since we are considering a *continuous* fluid of collisionless particles; rather, successive shell-crossings by particles at different phases in the orbits have filled the phase space. An interesting point is that, so long as the evolution remains self-similar, this phase-space diagram does not change, since every new particle follows the same trajectory after turning around. Of course, the figure applies only after enough orbits have occurred to populate the branches shown here. Many orbits (an infinite number) have branches not shown in Figure 6, but only a limited region of phase space can be occupied in any real physical system of finite age. Although the similarity solution traces a smooth curve in the phase-space diagram, finite velocity dispersion, angular momentum, and, eventually, two-body encounters will lead to the filling of whole areas of the phase plane.

The nondimensional mass distribution $M(\lambda)$ derived from the self-similar trajectory $\lambda(\xi)$ using equation (4.3) is shown in Figure 7 and is tabulated in Table 4. For $\lambda > 0.364$ no shell-crossing occurs, and M is the same as that given in Figure 1*b* for cold accretion. The mass dips at every maxi-

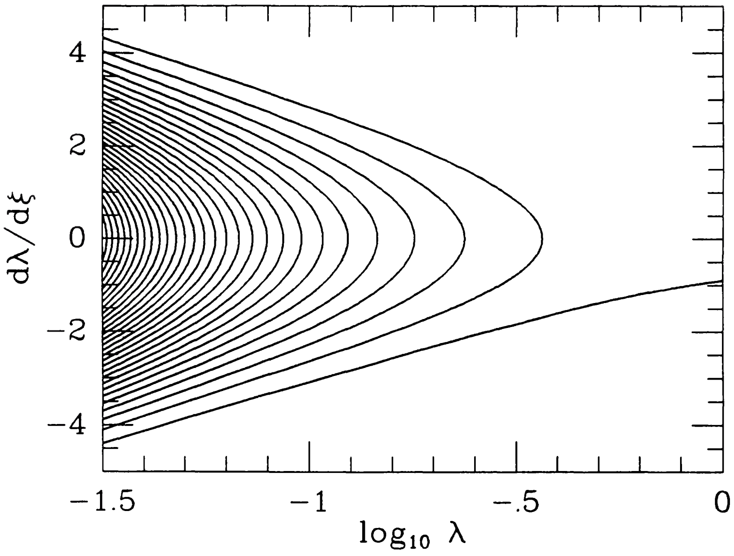

FIG. 6.—Phase-space diagram for the collisionless infall similarity solution. The nondimensional velocity of a particle is $V(\xi) = d\lambda/d\xi + (8/9)\lambda$, where λ is the nondimensional radius (eq. [2.9]). Each branch of the phase curve corresponds to a single orbit in Fig. 5. A particle travels along the entire curve after first turning around; equivalently, at a fixed time all portions of the curve are occupied by different particles. Only a small portion of the phase plane is shown here to avoid excessive cluttering.

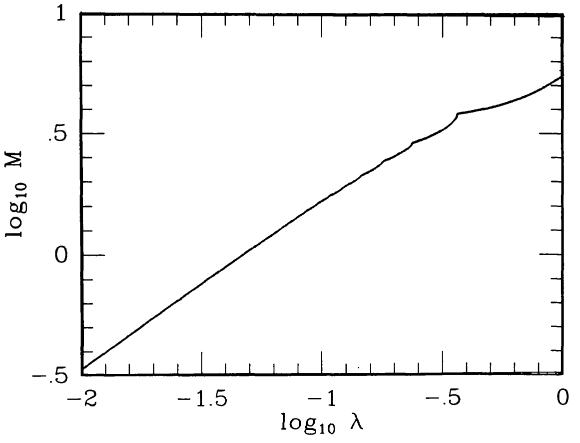

FIG. 7.—Nondimensional mass distribution in the collisionless infall similarity solution. For $\lambda \ll 1$, $M \propto \lambda^{3/4}$. Units are provided by eqs. (2.9) and (3.2).

mum λ_k in the trajectory (Fig. 5), since at these turning points the mass is reduced by shell-crossing. It will be shown below that the density becomes infinite at the λ_k, which are thus caustic surfaces. The magnitude of the decrease in mass diminishes the higher the order k of the caustic (k increases with ξ in the trajectory) since, as argued above, the nondimensional mass decreases as $e^{-(2/3)\xi}$ along the trajectory. Only the first few caustics are evident in $M(\lambda)$, although they show up more readily in the density.

The most important result shown in Figure 7 is probably not the presence of caustics, but that M approaches a power law for $\lambda \ll 1$. The numerical results show that

$$M \approx 11.2\lambda^{3/4}, \qquad D \approx 2.79\lambda^{-9/4}, \qquad \lambda \ll 1, \qquad (4.5)$$

TABLE 4

MASS AND DENSITY DISTRIBUTIONS IN THE COLLISIONLESS INFALL SIMILARITY SOLUTION

λ	M	D	λ	M	D
0.020	0.561	1.58(+4)	0.520	4.10	2.51
0.040	0.909	4.41(+3)	0.540	4.14	2.41
0.060	1.20	1.09(+3)	0.560	4.18	2.32
0.080	1.45	5.19(+2)	0.580	4.23	2.24
0.100	1.67	3.12(+2)	0.600	4.27	2.16
0.120	1.88	2.53(+2)	0.620	4.32	2.09
0.140	2.06	1.70(+2)	0.640	4.37	2.02
0.160	2.24	9.69(+1)	0.660	4.42	1.96
0.180	2.45	5.42(+1)	0.680	4.47	1.91
0.200	2.56	5.16(+1)	0.700	4.53	1.86
0.220	2.70	5.57(+1)	0.720	4.58	1.81
0.240	2.92	2.23(+1)	0.740	4.64	1.77
0.260	3.00	2.10(+1)	0.760	4.70	1.72
0.280	3.09	2.02(+1)	0.780	4.76	1.68
0.300	3.19	2.00(+1)	0.800	4.82	1.65
0.320	3.31	2.08(+1)	0.820	4.89	1.61
0.340	3.45	2.41(+1)	0.840	4.95	1.58
0.360	3.68	4.75(+1)	0.860	5.02	1.55
0.380	3.85	3.60	0.880	5.09	1.53
0.400	3.88	3.38	0.900	5.16	1.50
0.420	3.91	3.19	0.920	5.24	1.47
0.440	3.95	3.03	0.940	5.31	1.45
0.460	3.98	2.88	0.960	5.39	1.43
0.480	4.02	2.74	0.980	5.47	1.40
0.500	4.06	2.62	1.000	5.55	1.39

NOTE.—Units are given in eqs. (2.9) and (3.2).

where the nondimensional density D follows from differentiating M in equation (4.6) below. The power-law behavior agrees with equation (3.12), which was shown in § III to hold for a $\gamma > 4/3$ collisional gas. Indeed, one may see by comparing Figures 7 and 8 with Figure 2 that, provided the caustics are

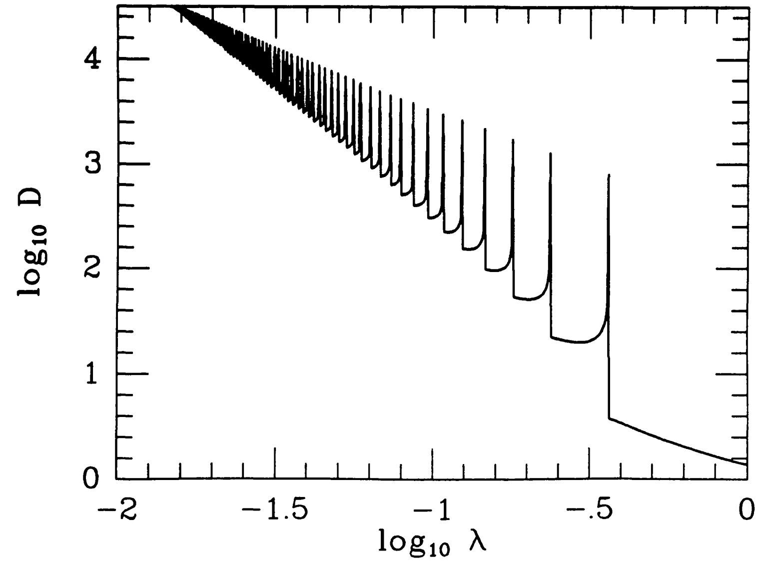

FIG. 8.—Nondimensional density distribution in the collisionless infall similarity solution, with units given by eqs. (2.9) and (3.2). The density becomes infinite at the many caustics, although it is limited here to finite values because of finite resolution in log λ. (The slope of the line of peaks has no particular significance.) For $\lambda \ll 1$, $D \propto \lambda^{-9/4}$.

TABLE 5

PARAMETERS OF THE CAUSTICS IN THE COLLISIONLESS INFALL SIMILARITY SOLUTION

k	ξ_k	λ_k	$(d^2\lambda/d\xi^2)_k$
1	0.988	0.364	−6.35
2	1.46	0.236	−11.6
3	1.76	0.179	−16.9
4	1.98	0.145	−22.4
5	2.15	0.123	−28.1
6	2.30	0.108	−33.8
7	2.43	0.096	−39.6
8	2.54	0.086	−45.6
9	2.64	0.079	−51.5
10	2.73	0.073	−57.6

smoothed over, the collisionless and $\gamma = 5/3$ collisional solutions have very similar Eulerian fluid distributions. The coefficients in equation (4.5) agree closely with those for a $\gamma = 5/3$ gas, $\tilde{M}(0)$ and $\tilde{D}(0)$ in Table 3. One might have expected the collisionless solution to behave more like the $\gamma = 3$ collisional solution, corresponding to a gas with only one translational degree of freedom, since the collisionless gas particles move only in radius and have no internal degrees of freedom. The $\gamma = 3$ solution has shock radius $\lambda_s = 0.600$, however, compared with $\lambda_s = 0.339$ for $\gamma = 5/3$ and $\lambda_1 = 0.364$ for the first caustic in the collisionless solution. Evidently the relaxation occurring in the collisionless gas is nearly as effective in generating "entropy" as a $\gamma = 5/3$ shock. The fact that the collisionless gas obeys even the same power law has important implications for the physical interpretation of the similarity solutions, which will be discussed below.

The nondimensional density $D(\lambda)$ defined in equation (3.2) follows from equation (4.3):

$$D(\lambda) = \frac{1}{3\lambda^2}\frac{dM}{d\lambda} = \frac{2}{9}\frac{M_{\rm ta}}{\lambda^2}\sum_i (-1)^i \exp\left(-\frac{2}{3}\xi_i\right)\left(\frac{d\lambda}{d\xi}\right)_i^{-1} . \tag{4.6}$$

The density is graphed in Figure 8 and is tabulated in Table 4. Equation (4.6) shows that D is singular at the caustics $\lambda = \lambda_k$, $k = 1, 2, \cdots$, etc., where $d\lambda/d\xi = 0$. Physically the density becomes infinite at these points because adjacent mass shells catch up with each other when $d\lambda/d\xi = 0$, compressing the matter between them. The abscissae ξ_k, ordinates λ_k, and second derivatives $(d^2\lambda/d\xi^2)_k$ evaluated at the maxima of $\lambda(\xi)$ are listed in Table 5 for $k \le 10$. From equation (4.5) it follows that just interior to a caustic, $0 < \lambda_k - \lambda \ll 1$, the density is given approximately by

$$D(\lambda) \approx \frac{2}{9}\frac{M_{\rm ta}}{\lambda_k^2}\exp\left(-\frac{2}{3}\xi_k\right)\left[-\frac{1}{2}\left(\frac{d^2\lambda}{d\xi^2}\right)_k\right]^{-1/2} \times (\lambda_k - \lambda)^{-1/2} . \tag{4.7}$$

Notice from Figure 8 that for $\lambda \ll 1$ the caustics are scarcely noticeable and the power-law behavior $D \propto \lambda^{-9/4}$ (eq. [4.5]) dominates.

A secondary density maximum occurs in the envelopes of many clusters of galaxies (Oemler 1974). Several theoretical explanations have been advanced for this feature (e.g., Dekel and Shaham 1980, and references therein). Recently, Farouki, Hoffman, and Salpeter (1983) showed that the secondary density maximum can move outward. They showed kinematically from velocity gradients how this feature propagates but do not give a dynamical explanation for the motion. Although their simulations did not include secondary infall, it seems plausible that this density peak may form and propagate the same way as do the caustics in the secondary infall similarity solution; that is, as a sort of compression wave peaking where adjacent mass shells turn around and catch up with each other. If the initial collapse is centrally condensed (central condensation quickly occurs through mass segregation with the small numbers of particles used in their simulations), then it is not unreasonable to expect collapse and relaxation to proceed from smaller to larger scales; hence caustics or other features would tend to move outward even in the absence of secondary infall. Farouki *et al.* point out that without secondary infall the feature is transient and thus can be used to estimate the age of a system showing such a feature. However, there is no *a priori* reason why infall should not *continue* after the initial collapse, in which case their arguments cannot be applied, since features in the density profile are then always present, as Figure 8 shows.

The secondary density maximum may in fact be the outermost caustic forming during secondary infall. The caustic occurs at a radius $0.364 r_{\rm ta} = 1.09 r_G$, where $r_G \equiv -Gm_{\rm ta}^2/2E_{\rm ta} = r_{\rm ta}/3$ is the "gravitational radius" based on the mass and binding energy interior to the turnaround radius. The caustic position may be specified alternatively by noting that the density immediately ahead of the caustic is 3.78 times the Einstein–de Sitter (unperturbed) density $\rho_{\rm H}$ (Fig. 8). Although one may expect to see more than one density peak, projection onto the plane of the sky, finite velocity dispersion, and other effects make all but the strongest caustic difficult to detect.

The caustics occur only if the infalling matter has zero velocity dispersion, or equivalently if the locus of particles turning around at a given time is a sphere, with no spread in radius. There must be a finite velocity dispersion in any real collisionless gas, which will lead to a smearing of the caustics, since the trajectories are then perturbed so that the particles do not all turn around at the same nondimensional radii. Nonetheless the caustics are suggestive of the sharp shells observed around giant elliptical galaxies (Malin and Carter 1980; Schweizer 1980)—hence secondary infall offers a possible explanation of the shells. The similarity solution predicts that the shells should be spherical and radially spaced in proportion to the λ_k listed in Table 5, since the kth caustic ($k = 1$ is the outermost caustic) is at a fraction λ_k of the current turnaround radius. Moreover, equation (4.4) shows that the material in the caustics, as well as the caustics themselves, moves outward with velocity

$$v_{\rm caustic} = \frac{8}{9}\frac{r_{\rm caustic}}{t}, \qquad (4.8)$$

or 4/3 times the Hubble velocity at the caustic. These predictions offer a strong test of the infall theory.

The shells observed by Malin and Carter (1980) around the normal elliptical galaxies NGC 1344 and NGC 3923 are sharp-edged, concentric, and approximately spherical (although they are flattened slightly in the same direction as the galaxies), so they may be evidence of self-similar secondary infall. However, the caustics are incorrectly spaced: e.g., in NGC 3923, the observed shells have radii of 20, 5.9, 3.3, and 2.2 arc minutes (Malin and Carter 1980). From Table 5 the ratio of the radii of the two outer shells should be 1.5, instead of the observed 3.4. This difference may be explained if the matter outside the original perturbation is not as tightly bound as in the similarity solution; this is the case if $\Omega < 1$ or $\Omega = 1$ but the initial density perturbation is partially compensated by decreased density at large distances, so that the excess mass $m_x(r) \to 0$ as $r \to \infty$. In either of these cases a given mass shell turns around later than it does in the $\Omega = 1$, finite mass excess case, and the caustic ratios are increased. The density distribution is then also steeper than $\rho \propto r^{-2.25}$. While the solutions have been obtained in this paper only for the hatbox perturbation in an $\Omega = 1$ universe, it is plausible that these other cases can reproduce the observed ellipticals; a corollary is that the shell spacing ratios should be larger, the steeper the halo density profile.

Malin, Quinn, and Graham (1983) have given an alternative explanation of the shells around ellipticals based on galaxy mergers. For cases where the shells are not spherically symmetric and there is evidence of a collision, e.g., NGC 5128, the merger hypothesis is more likely to be correct. The biggest observational difference between the merger and secondary infall models is that the infall picture predicts concentric spherical shells, while the merger picture predicts that the caustics are interleaved, with the caustic radii alternating on opposite sides of the galaxy. The physics of the two mechanisms is identical, however: caustics form where mass shells catch up with each other. Indeed, the merger of a small galaxy with a larger one may be considered a special case of infall, although it is clearly not self-similar and the caustics will eventually disappear (as they do for secondary infall after the infall stops).

It should be noted that finite velocity dispersion in the infalling gas will not necessarily affect the central power-law form of the mass distribution given by equation (4.5), even though it smooths the caustics. Both the coefficient and exponent in equation (4.5) will be unchanged by a superposition of random velocities provided only that spherical symmetry still holds and that the velocities are purely radial. If the particles are given angular velocities, however, they will not pass through the center, in which case the density distribution turns over at small λ. (This fact was used as a computational artifice to avoid the singularity at the center.)

The main utility of the nondimensional trajectory $\lambda(\xi)$ is that it gives a Lagrangian description of all the particles in the collisionless similarity solution. This description is necessary to obtain the mass $M(\lambda)$ using equation (4.3) and thus to obtain the similarity solution. However, while nondimensionalizing the trajectory $r(t)$ in terms of the current turnaround radius $r_{\rm ta}(t)$ is necessary to obtain and study the global properties of the solution, it obscures the details of the particle motion which lead, e.g., to equation (4.5). Thus we now restrict our attention to the motion of a single particle, for which it is better to nondimensionalize the radius in terms of the fixed turnaround radius $r'_{\rm ta}$ of the particle.

Figure 9 shows the first several orbits of a single particle in the collisionless infall similarity solution, with units provided by the particle's own turnaround time and radius. This figure

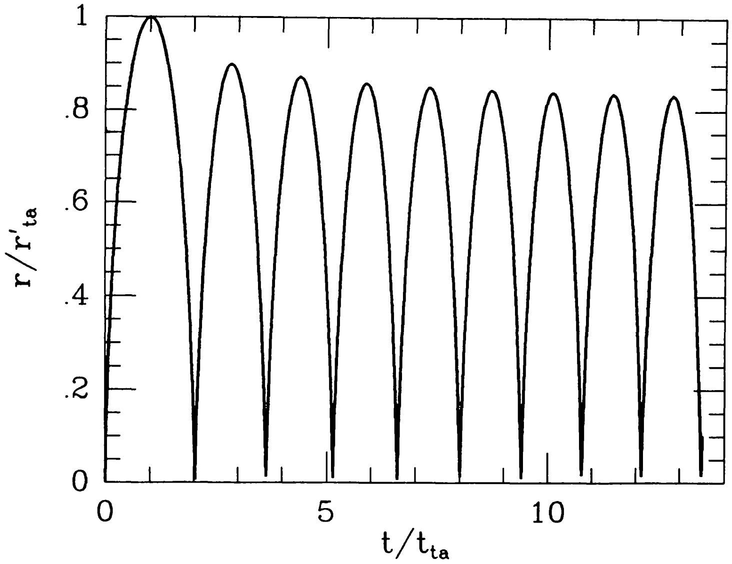

FIG. 9.—Trajectory in the collisionless infall similarity solution. Units are provided by the fixed turnaround time and radius of the particle, in contrast to Fig. 5. After a few orbits during which the particle undergoes violent relaxation, it settles down to a periodic orbit. This trajectory is followed by every particle; only the units change. Compare with the collisional trajectories of Fig. 4.

may be compared directly with Figure 4 for collisional infall and cold accretion. Unlike Figure 5, Figure 9 does not show the simultaneous positions of all particles in the similarity solution, but it reveals a surprising fact. *Individual orbits become periodic after a few crossing times.* A hint of this result was given in Figure 5 with the observation that the maximum nondimensional radius λ_k decreases with time, and that the orbit period measured in ln t decreases, but it is made manifest in Figure 9. Thus there is a twofold self-similarity: every particle trajectory looks like every other when scaled appropriately in time; moreover, a single particle trajectory looks like itself when translated in time, when the orbit becomes periodic.

At first this result seems to violate intuitive notions that the orbit radius should continue to decrease as more matter is added via infall (with the preservation of an adiabatic invariant for the orbit), as argued by Gunn (1977), but there is a simple derivation showing that this argument is incorrect. From equations (2.7), (2.9), (3.2), and (4.5), the mass interior to $r \ll r_{ta}(t)$ at time t is

$$m(r,t) = \tfrac{4}{3}\pi\rho_H r_{ta}^3 M(\lambda) \propto t^{2/3}\lambda^{3/4} \propto t^{2/3}(rt^{-8/9})^{3/4} \propto r^{3/4} \tag{4.9}$$

and is therefore independent of time. After a few orbits, so that $\lambda = r/r_{ta}(t) \approx (t/t_{ta})^{-8/9} \ll 1$, the mass distribution (and hence force field) seen by the particle is static, and the orbit is thus periodic.

The reader may now well ask how $m(r,t)$ can be time independent—surely infall must increase the mass interior to any radius? The answer, shown in equation (4.9), is no, so long as $m(r,t)$ is self-similar and $M(\lambda) \propto \lambda^{3/4}$. The physical explanation is that mass shells falling in long after the turnaround time of the particle under consideration pass by so quickly that they add a negligible amount to the mass already interior to the particle. The mass is therefore dominated by shells turning around at about the same time as the particle or earlier. The mathematical expression of this is provided by equation (4.3) for $M(\lambda)$, where, for $\lambda \ll 1$, all the terms nearly cancel except the last one; the numerical solution shows that about 56% of the contribution to M comes from the last term for $\lambda \ll 1$. From this we can derive the relation $M(\lambda) \propto \lambda^{3/4}$, as follows. Assume that the maximum radius of the particle orbit is not constant but varies as $r_{max} \propto t^{\alpha}$ for some α. Then the envelope of $\lambda(\xi)$ is $\lambda \propto e^{(\alpha-8/9)\xi}$, so the last term in the series (4.3) has $\xi_i = (\alpha - 8/9)^{-1} \ln \lambda + \text{const}$. Assuming that the last term either dominates the sum or is at least proportional to it gives

$$M(\lambda) \propto \lambda^{-(2/3)(\alpha-8/9)^{-1}}. \tag{4.10}$$

Arguing now along the lines of equation (4.8), the dimensional mass interior to the particle at its maximum radius is

$$\begin{aligned} m(r_{max}, t) &\propto t^{2/3}\left(r_{max}\, t^{-8/9}\right)^{-(2/3)(\alpha-8/9)^{-1}} \\ &\propto t^{2/3}\left(t^{\alpha-8/9}\right)^{-(2/3)(\alpha-8/9)^{-1}} \propto t^0 \end{aligned} \tag{4.11}$$

and is constant. The same is true for the mass within any constant fraction of r_{max}. Thus the mass distribution seen by the particle is constant, from which it follows that $\alpha = 0$, since a radial orbit in a static force field is periodic, and so $M \propto \lambda^{3/4}$, from equation (4.10). The periodicity of the orbit is consistent with the power-law form $M(\lambda) \propto \lambda^{3/4}$ and vice versa.

The physical interpretation of the similarity solution given by Figure 9 is very interesting. After a particle first turns around at $t = t_{ta}$, it sees a changing force field at $r \sim r_{ta}(t)$, since M is not proportional to $\lambda^{3/4}$ for $\lambda \sim 1$ (see Fig. 7). The energy of the orbit is thus not a conserved quantity, and the particle undergoes violent relaxation (Lynden-Bell 1967). The maximum radius of the orbit decreases during this period, although not by much. After a few crossing times the maximum orbit radius is much less than the turnaround radius at that time, since $r_{\mathrm{ta}}(t)$ continues to increase as $t^{8/9}$, so that the orbit is restricted to $\lambda \ll 1$ (see Fig. 5), where the nondimensional mass approaches the power law given in equation (4.5). The gravitational field seen subsequently by the particle is static, and the orbit becomes periodic. There is one subtlety which should be clarified here. As successive mass shells are added, the depth of the central potential well continues to increase; but the potential gradient, given by $-Gm/r^2$, is unchanging at fixed r. Thus, strictly speaking, the energy of a particle continues to decrease with infall, although this energy change is illusory since it does not affect the motion of the particle. If the potential is measured from the center, rather than from infinity, the orbit-averaged gravitational energy per unit mass $\langle W \rangle = -\int Gm(r,t)/r^2\,dr$ is constant, since $m(r,t)$ is independent of time after several orbits have elapsed. The standard form of the virial theorem, $\langle 2T + W \rangle = 0$, is then satisfied.

Although the motion of a single particle soon approaches a steady state, the solution as a whole is self-similar, not steady. The relaxation process described above occurs for each new mass shell which turns around, with the turnaround radius increasing according to equation (2.7). The similarity solution has *continual* violent relaxation because new particles are continually added which need to be virialized. The relaxation does not affect the matter distribution at small radii, however, because particles there have already relaxed to periodic orbits. Thus secondary infall is a process of building up a dynamically relaxed halo with density distribution $\rho \propto r^{-2.25}$. The relation of this self-similar relaxation process to the violent relaxation described by Lynden-Bell (1967), which leads instead to $\rho \propto r^{-2}$, is discussed at the end of this section.

Since virialization changes the structure of only the outermost parts of the similarity solution, it is clear that once infall stops, either because $\Omega < 1$ and there is a last bound shell, or because all the matter previously available for infall has been accreted elsewhere, the structure of the virialized object will not change—it simply stops growing. The density profile will necessarily steepen in the outer parts—Gott (1975) showed that a $\rho \propto r^{-4}$ tail forms when $\Omega \ll 1$—but the profile $\rho \propto r^{-9/4}$ will be unchanged in the inner parts.

Besides giving a physical interpretation of the collisionless similarity solution, Figure 9 suggests a computational algorithm which has been used to increase the accuracy of the solution. The integration of equation (4.1) as described above is of limited accuracy because the trajectory depends on the mass distribution at small radii. For $\lambda \ll 1$, obtaining M from equation (4.3) requires carrying the series out to $\sim \lambda^{-9/8}$ terms; thus the trajectory $\lambda(\xi)$ must be computed to large ξ. For example, evaluating M at $\lambda = 0.01$ requires computing approximately 80 orbits. As Figure 9 shows, much of this effort is needless because the orbit quickly becomes periodic. The algorithm adopted was therefore to integrate about 10 orbits directly and to assume that later orbits are exactly periodic. Equation (4.3) was still used to obtain the nondimensional mass, except at very small radii ($\lambda < 5 \times 10^{-3}$), where it was assumed that $M \propto \lambda^{-3/4}$. The trajectory was integrated in the dimensional form $r(t)$ using the equation of motion (2.1), with $m = m(r,t)$ given by equation (3.2); this is equivalent mathematically to integrating equation (4.1) for the nondimensional trajectory $\lambda(\xi)$ and changing variables to $r/r'_{\mathrm{ta}} = \lambda e^{(8/9)\xi}$. The dimensional form chosen for the integration is computationally superior because the maximum λ decreases exponentially with ξ, and so errors grow more rapidly when integrating equation (4.1) than equation (2.1). Ten iterations of the trajectory were computed, at the end of which $r(t)/r'_{\mathrm{ta}}$ was changing by less than 1% per iteration. The final trajectory is that shown in Figure 9.

Global checks of the solution were provided by energy conservation (eq. [3.8], with $d_s \to 3\pi/4$) and the nondimensional virial theorem (eq. [3.11], with $\lambda_s \to 1$, $D_2 \to D_{\mathrm{ta}}$, and $V_2 \to 0$). The thermal energy u is zero because all the particle motions are included when calculating the kinetic energy t. The energy integrals in equation (3.9) were calculated numerically for particles interior to the turnaround radius using cubic splines quadrature. The integration variable was taken to be the Lagrangian variable ξ, so that (cf. eq. [4.3])

$$dM = \frac{2}{3} M_{\mathrm{ta}} e^{-(2/3)\xi}\, d\xi . \tag{4.12}$$

The nondimensional kinetic and gravitational energies computed from the similarity solution are

$$\frac{t}{E} = 0.92, \qquad \frac{w}{E} = -1.92, \tag{4.13}$$

where $E \equiv |t + w| = (1/3)(3\pi/4)^4$ from equation (3.8). The virial theorem (3.11) was satisfied with a relative error of 1%, but energy conservation (3.8) was satisfied to only 5%. These inaccuracies are due to the slow convergence ($\sim \lambda^{1/2}$ as $\lambda \to 0$) of the energy integrals in equation (3.9) and are believed to be much larger than the true errors in the computed orbits. The virial theorem checks better than energy conservation because, for small λ, the particle orbits are relaxed and the contributions to the energy integrals satisfy the ordinary virial theorem, $2t + w = 0$, and thus contribute no error to the virial theorem (3.11). Note from equation (4.13) that the entire system within the turnaround radius is not in virial equilibrium; since $2t + w < 0$, the radius of the shells currently turning around must decrease before equilibrium can be achieved. It is interesting, however, how close the system actually is to being in virial equilibrium; this offers an alternative explanation for why the particle orbits in Figure 9 return nearly all the way to the initial turnaround radius.

Table 6 lists the periods and maximum radii for the first 10 orbits. Note that the maximum radius is defined here by $dr/dt = 0$; since $\lambda \propto rt^{-8/9}$, this is not the same as $d\lambda/d\xi = 0$, so the caustic radii λ_k listed in Table 5 do not correspond exactly with the r_k in Table 6. The caustics move outward with velocity given by equation (4.8), while a particle has zero velocity by definition at a maximum r_k. Table 6 shows that relaxation occurs rapidly, with the orbit parameters changing by $\lesssim 2\%$ after 10 orbits. It is interesting how little the

TABLE 6

MAXIMUM RADII AND ORBITAL PERIODS IN THE COLLISIONLESS INFALL SIMILARITY SOLUTION

k^a	r_k/r'_{ta}	P_k/t_{ta}
0	1.00	2.03
1	0.896	1.60
2	0.869	1.49
3	0.854	1.44
4	0.845	1.40
5	0.838	1.38
6	0.833	1.35
7	0.830	1.34
8	0.826	1.33
9	0.823	1.32
10	0.821	1.31

[a] $k = 0$ corresponds to the initial "orbit" from $t = 0$ to the first passage through the center.

TABLE 7

LIMITING PERIODIC ORBIT IN THE COLLISIONLESS INFALL SIMILARITY SOLUTION

t/t_{ta}	r/r'_{ta}	$v/(r'_{ta}/t_{ta})$
0	0	∞
0.061	0.234	2.66
0.126	0.383	1.99
0.191	0.498	1.57
0.256	0.590	1.26
0.321	0.663	1.01
0.386	0.720	0.768
0.451	0.763	0.559
0.516	0.793	0.363
0.581	0.811	0.174
0.642	0.816	0
0.646	0.816	−0.011
0.711	0.810	−0.197
0.776	0.790	−0.386
0.841	0.759	−0.584
0.906	0.714	−0.796
0.971	0.655	−1.03
1.036	0.576	−1.30
1.101	0.485	−1.62
1.166	0.366	−2.06
1.231	0.211	−2.79
1.289	0	$-\infty$

maximum radius decreases as a result of relaxation; previous investigators (e.g., Gunn 1977) assumed it would decrease by half. As shown above, this small change may be viewed as a consequence of the near-virial equilibrium already existing for the system as a whole at turnaround, or alternatively because the mass distribution $m(r,t) \propto r^{3/4}$ is constant for r not much less than $r_{ta}(t)$, so that the particle energy changes only during the outer courses of the first few orbits. The limiting periodic orbit is listed in Table 7, where the phase has been chosen so that $r = 0$ at $t = 0$. The time-averaged radius of this orbit is

$$\langle r \rangle = 0.58 r'_{ta}. \qquad (4.14)$$

This is somewhat larger than the settling radius for a $\gamma = 5/3$ collisional fluid particle, $r_\infty = 0.433 r'_{ta}$, but is fairly close to the shock radius r_s, from Table 3. These comparisons are of interest because the collisionless and $\gamma = 5/3$ collisional solutions were shown above to be similar in several ways; e.g., they have approximately the same mass distribution.

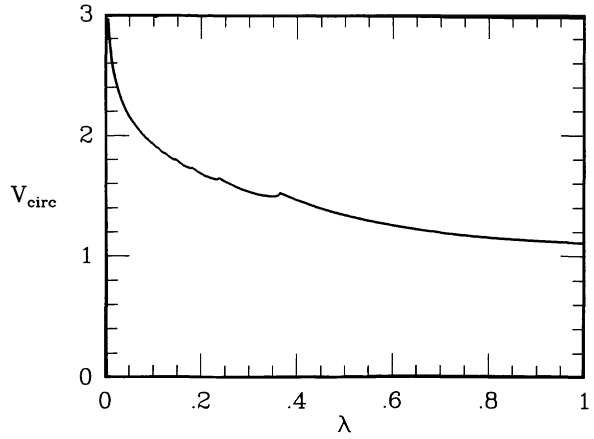

FIG. 10.—The nondimensional circular rotation velocity (eq. [4.15]) obtained from the self-similar collisionless mass distribution, plotted vs. radius. For $\lambda \ll 1$, $V_{\rm circ} \propto \lambda^{-1/8}$.

From equation (4.5), it follows that both the radial velocity dispersion and the circular rotation velocity scale as $r^{-1/8}$ and are independent of time for $r \ll r_{ta}(t)$ in the similarity solution. The nondimensional circular rotation velocity $V_{\rm circ}(\lambda)$ is defined by

$$v_{\rm circ}^2 \equiv \frac{Gm(r,t)}{r}, \qquad v_{\rm circ} \equiv \frac{r_{ta}}{t} V_{\rm circ}(\lambda), \qquad (4.15)$$

and is plotted versus the nondimensional radius λ in Figure 10. Physically, Figure 10 gives the rotation curve for test particles moving in the potential determined by the collisionless mass distribution. The rotation curve is relatively flat, with $V \propto \lambda^{-1/8}$ for $\lambda \ll 1$, compared with the Keplerian $V \propto \lambda^{-1/2}$. Secondary infall thus (nearly) offers a possible way of explaining the flatness of spiral galaxy rotation curves (e.g., Rubin, Ford, and Thonnard 1980), a fact first shown by Gunn (1977). In any real galaxy, since infall did not begin at $t = 0$, the density must become uniform sufficiently close to the center (inside the core radius), in which case $V_{\rm circ}$ will turn over at small λ and should then look more like a real galaxian rotation curve. Numerical simulations have given mixed results (e.g., Dekel, Kowitt, and Shaham 1981; Pryor and Lecar 1983), but the similarity solution is correct outside the center provided that infall is roughly spherical and continues for more than a few crossing times after the initial perturbation collapses. Notice that the caustics produce small bumps in $V_{\rm circ}$. For $\lambda > 1$, the self-similar mass distribution approaches that of unperturbed Hubble flow, $M = \lambda^3$ (with an excess given by eq. [2.17]), so $V_{\rm circ}$ approaches the Hubble velocity $(2^{1/2}/3)\lambda$. Of course, a particle at this distance is no longer associated with the central object, and the concept of the circular velocity is sensible only for $\lambda < 1$.

Bahcall, Schmidt, and Soneira (1982) showed that it is not necessary to have a halo density profile as flat as $\rho \propto r^{-2}$ to produce a flat galaxian rotation curve. They found that a halo distribution as steep as $\rho \propto r^{-2.7}$ can produce flat spiral rotation curves for $40 < r < 60$ kpc when other components are considered. A halo density exponent of 2.25 is also consistent with a flat rotation curve for reasonable component parameters (J. Bahcall, private communication).

Lynden-Bell (1967) argued in a classic paper that violent relaxation leads to a quasi-equilibrium Maxwellian distribution with temperature proportional to particle mass, i.e., constant velocity dispersion. For a gas of equal-mass particles this gives an isothermal sphere, with $\rho \propto r^{-2}$. It is interesting that the self-similar violent relaxation found in this section leads instead to $\rho \propto r^{-2.25}$. The difference in exponents is not surprising, considering that the self-similar distribution function is anisotropic, with radial orbits only, and depends also on position, with velocity dispersion behaving as $r^{-1/8}$ for $r \ll r_{\rm ta}(t)$. The fact that the similarity solution is evolving is not responsible for the differences since, as shown above, particles relax in a few crossing times and are thereafter unaffected by the infall of more mass, which changes only the scale of the system. The reason for the difference is apparently that Lynden-Bell coarse-grained the distribution function and assumed that every volume of phase space is equally likely to be occupied, subject to constraints given by conservation of total energy and the Vlasov equation (conservation of phase-space density). Here the fine-grained distribution function is obtained instead (see the phase-space diagram Fig. 6), and it is clear that even after coarse-graining, not every phase volume satisfying the energy constraint is equally likely to be occupied. Stated in another way, Lynden-Bell assumed that the only isolating integrals of motion are total energy and phase-space density. Since only radial orbits are allowed here, however, there is at least one additional isolating integral. It would be interesting to see if a set of integrals can be found such that the self-similar distribution found here can be derived using equilibrium statistical mechanics. If not, the similarity solutions show that even in the absence of collisions, which drive the evolution away from equilibrium, purely gravitational processes, including violent relaxation, do not necessarily lead to the "most probable state" found by Lynden-Bell.

An alternative way of seeing that self-similar relaxation should not lead to an isothermal sphere is to note that, in the similarity solution, after collisionless particles relax, they retain a complete "memory" of their initial conditions (see Fig. 9). While self-similar relaxation mixes the phases of particles turning around at different times, it does not phase-mix particles turning around at the same time. Self-similar relaxation is not "complete" and thus heuristically should not lead to a density profile as flat as $\rho \propto r^{-2}$. It is uncertain to what extent the addition of angular momentum (i.e., nonradial orbits) will change this result, but the self-similar relaxation probably gives a better description than violent relaxation of the process actually taking place in the formation of galaxy and cluster halos.

V. COLLISIONLESS INFALL AND SHOCKED ACCRETION

Similarity solutions have been found in the preceding two sections for secondary infall of a collisional gas settling into the center of an accreting gas cloud, and for a gas of collisionless particles, which oscillate about the center and relax to periodic orbits. Similarity solutions clearly also exist for any combination of the two, provided that the total density adds up to $\Omega = 1$ far outside the turnaround radius. While it would be tedious and not particularly enlightening to work out the solutions for all possible cases, there is one mixture which is a reasonable possibility cosmologically and for which the similarity solution is easy to derive. This is the case of a collisional (e.g., baryon) gas with density parameter $\Omega_b \ll 1$ moving in the potential of the $\Omega = 1$ collisionless solution for, e.g., massive neutrinos. The physical motivation for studying this case is the possibility that galaxy halos are made of nonluminous collisionless matter, with a small amount of gas added to form stars providing the luminosity. The hope is thereby to explain the large mass-to-light ratios inferred in galactic halos, small groups, and clusters (the "missing mass" problem).

Since $\Omega_b \ll 1$ is assumed and the collisionless particles are unaffected by pressure forces, the motion of the collisionless component is given by the similarity solution derived in § IV; the motion of the collisional component is derived in this section. The gravitational potential into which the collisional fluid falls is given by the nondimensional mass distribution $M_x(\lambda)$ of the collisionless gas. The collisionless fluid variables will be written with a subscript x in this section to distinguish them from the collisional fluid variables, written without subscript.

The collisional fluid variables are nondimensionalized here as in equation (3.2), except that $\rho_{\rm H}$ is multiplied by Ω_b. After being shocked, the collisional fluid must satisfy the dimensional and nondimensional fluid equations (3.3) and (3.4), with the replacements $m \rightarrow m_x$ in equation (3.3b) and $M \rightarrow M_x$ in equation (3.4b), since the collisional gas is not self-gravitating but moves instead in the potential of the collisionless component. The collisional fluid is required to satisfy the central boundary conditions (3.7); as in the purely collisional case considered in § III, a shock forms with radius $\lambda_s r_{\rm ta}(t)$, with λ_s fixed by requiring the central boundary conditions to hold.

The preshock motion of the collisional component differs from that in § III if the shock occurs interior to the outer caustic at λ_1 in the collisionless solution, since the mass distribution seen by the preshock gas is then no longer that of Figure 1*b*. This will turn out to be the case for all γ's of interest. However, since the preshock collisional gas is pressureless, its motion is identical with that of collisionless fluid shells turning around for the first time. It is therefore convenient to describe the shock position by ξ_s, obtained by inverting the relation $\lambda_s = \lambda(\xi)$, where $\lambda(\xi)$ is the nondimensional trajectory obtained in § IV for a collisionless particle (and that of a collisional fluid particle before it is shocked). The inversion is possible before the particle passes through the center; obviously a shock must form before then if the boundary conditions (3.7) are to be satisfied. The preshock mass is then just that for the collisionless case (eq. [4.3]), except that it is not diminished by shell-crossing:

$$M_1 = M_{\rm ta} \exp\left[-(2/3)\xi_s\right]. \qquad (5.1)$$

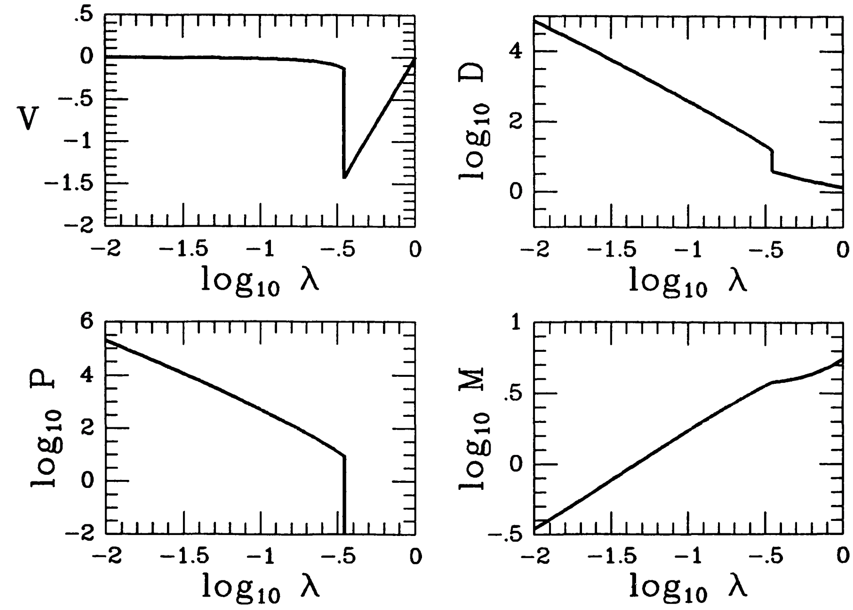

FIG. 11.—Self-similar accretion of a $\gamma = 5/3$, $\Omega_b \ll 1$ collisional gas moving in the potential of the $\Omega = 1$ collisionless solution. The velocity V, density D, pressure P, and mass M are plotted vs. radius λ, with units given by eqs. (2.9) and (3.2), with ρ_H reduced by a factor of Ω_b.

Similarly, the preshock density is

$$D_1 = \frac{1}{3\lambda_s^2}\left(\frac{dM}{d\lambda}\right)_s = -\frac{2}{9}\frac{M_1}{\lambda_s^2}\left(\frac{d\lambda}{d\xi}\right)_s^{-1}, \qquad (5.2)$$

and the preshock velocity (eq. [4.4]) and pressure are

$$V_1 = \left(\frac{d\lambda}{d\xi}\right)_s + \frac{8}{9}\lambda_s, \qquad P_1 = 0. \qquad (5.3)$$

The shock jump conditions (3.6) then give the initial values for numerical integration, in terms of the eigenvalue ξ_s (or λ_s). The eigenvalue is varied numerically until the central boundary conditions (3.7) are satisfied. The method of solution is almost identical with that discussed in § III, the only difference being the preshock boundary conditions and the source of the gravitational forces. Since it was seen in § IV that, aside from the caustics, which do not significantly affect the potential, the collisionless mass distribution is similar to that for the collisional solutions, we may anticipate that the motion of the collisional fluid in the collisionless potential will not be very different from that of a purely collisional fluid. This will be shown to be true for $\gamma > 4/3$.

The $\Omega_b \ll 1$ collisional solution obeys the local integrals of motion (2.27) and (3.10), since they do not depend on the gravitational potential. The virial theorem (3.11) provides a global check, where now the gravitational energy defined in equation (3.9) is computed with integrand $M_x dM/\lambda$. It is not easy to calculate analytically the energy within λ_s, however, because shell-crossing in the collisionless fluid changes the potential seen by the collisional component, so the global energy check equation (3.8) was not applied here.

The fluid equations (3.4) were integrated for the $\Omega_b \ll 1$ collisional gas with 500 points in radius for $\gamma = 5/3$, $3/2$, $7/5$, and $4/3$; the shock position λ_s was varied until the inner boundary conditions (3.7) were satisfied. The fluid variables were first transformed using equations (3.12), since an asymptotic analysis of equations (3.4), using $M_x \propto \lambda^{3/4}$ near $\lambda = 0$, showed that the solutions satisfying the central boundary conditions have the power-law form derived earlier. This result is independent of γ when the potential is provided by M_x, suggesting that the $\gamma = 4/3$ solution will be well-behaved here.

The local integrals (2.27) and (3.10) were satisfied nearly as well as in the purely collisional case of § III, and the virial theorem was satisfied to better than 1% in all cases. The solutions for $\gamma = 5/3$ and $4/3$ are plotted in Figures 11 and 12 and are tabulated in Tables 8 and 9. Table 10 collects the parameters of the solutions (cf. Table 3).

The $\Omega_b \ll 1$, $\gamma = 5/3$ solution is almost indistinguishable from the $\Omega = 1$, $\gamma = 5/3$ solution obtained previously, as may be seen by comparing Figures 2 and 11, or Tables 1 and 8. The only real difference is that the shock occurs slightly closer to the origin in the self-gravitating case. This similarity is to be expected based on the observation made above that the collisionless mass distribution $M_x(\lambda)$ is very like the $\Omega = 1$ collisional $M(\lambda)$ for $\gamma = 5/3$.

The $\Omega_b \ll 1$, $\gamma = 4/3$ solution behaves quite differently from the $\Omega = 1$, $\gamma = 4/3$ solution, however. A comparison of Figures 3 and 12 shows that when the gas is not self-gravitating, the solution satisfies equations (3.12) for the leading behavior at $\lambda = 0$, as was anticipated above from an examination of the fluid equations. The physical interpretation of the $\gamma = 4/3$ case now becomes clear: a self-gravitating gas sphere can decrease its total energy if $\gamma < 4/3$ by collapsing, and

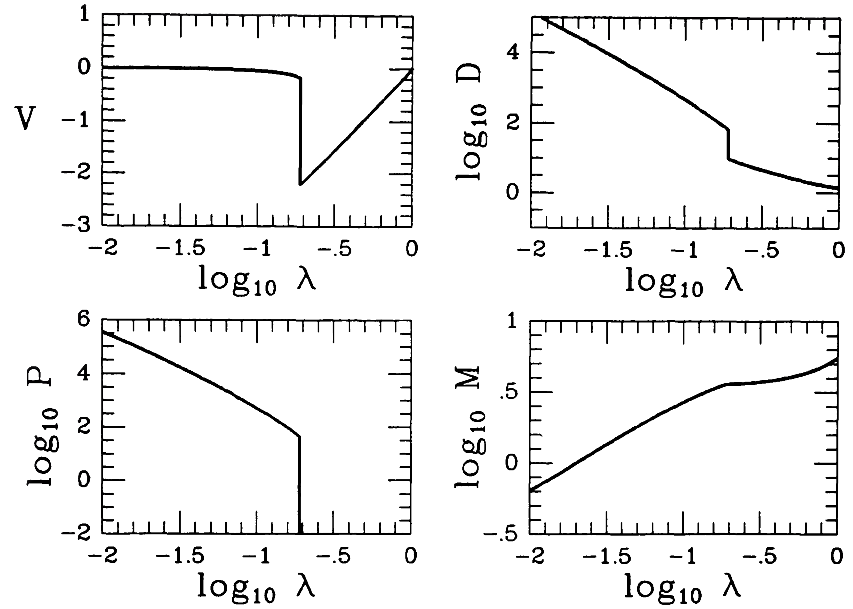

FIG. 12.—Same as Fig. 11, except $\gamma = 4/3$

TABLE 8

COSMOLOGICAL SELF-SIMILAR ACCRETION FOR $\Omega_b \ll 1$ COLLISIONAL GAS, $\gamma = 5/3$

λ	V	D	P	M
0..........	0	∞	∞	0
0.017......	−1.32(−3)	2.22(+4)	5.43(+4)	0.505
0.035......	−1.45(−3)	4.71(+3)	9.25(+3)	0.825
0.052......	−2.64(−3)	1.84(+3)	3.15(+3)	1.10
0.069......	−4.47(−3)	9.40(+2)	1.43(+3)	1.35
0.087......	−6.72(−3)	5.54(+2)	7.70(+2)	1.58
0.104......	−9.39(−3)	3.59(+2)	4.59(+2)	1.79
0.122......	−1.25(−2)	2.47(+2)	2.94(+2)	1.98
0.139......	−1.61(−2)	1.79(+2)	1.99(+2)	2.17
0.156......	−2.03(−2)	1.34(+2)	1.40(+2)	2.34
0.174......	−2.49(−2)	1.03(+2)	1.01(+2)	2.51
0.191......	−3.05(−2)	8.11(+1)	7.52(+1)	2.67
0.208......	−3.65(−2)	6.51(+1)	5.70(+1)	2.82
0.226......	−4.31(−2)	5.30(+1)	4.40(+1)	2.96
0.243......	−5.13(−2)	4.36(+1)	3.43(+1)	3.10
0.260......	−6.07(−2)	3.62(+1)	2.70(+1)	3.23
0.278......	−7.07(−2)	3.04(+1)	2.15(+1)	3.35
0.295......	−8.18(−2)	2.57(+1)	1.72(+1)	3.47
0.312......	−9.44(−2)	2.19(+1)	1.39(+1)	3.59
0.330......	−1.09(−1)	1.88(+1)	1.13(+1)	3.70
0.347^-....	−1.27(−1)	1.61(+1)	9.15	3.80
0.347^+....	−1.43	4.02	0	3.80

NOTE.—Units are given in eqs. (2.9) and (3.2), with $\rho_H \rightarrow \Omega_b \rho_H$. The potential is given by the collisionless infall similarity solution.

TABLE 9

COSMOLOGICAL SELF-SIMILAR ACCRETION FOR $\Omega_b \ll 1$ COLLISIONAL GAS, $\gamma = 4/3$

λ	V	D	P	M
0..........	0	∞	∞	0
0.009......	−5.35(−4)	1.61(+5)	4.44(+5)	0.581
0.019......	−1.34(−3)	3.23(+4)	7.20(+4)	0.946
0.028......	−2.80(−3)	1.23(+4)	2.39(+4)	1.25
0.038......	−4.99(−3)	6.07(+3)	1.06(+4)	1.51
0.047......	−7.97(−3)	3.46(+3)	5.51(+3)	1.74
0.057......	−1.18(−2)	2.16(+3)	3.18(+3)	1.95
0.066......	−1.62(−2)	1.44(+3)	1.97(+3)	2.14
0.076......	−2.14(−2)	1.01(+3)	1.29(+3)	2.31
0.085......	−2.74(−2)	7.34(+2)	8.80(+2)	2.47
0.095......	−3.41(−2)	5.49(+2)	6.21(+2)	2.62
0.104......	−4.18(−2)	4.20(+2)	4.49(+2)	2.75
0.114......	−5.04(−2)	3.27(+2)	3.32(+2)	2.88
0.123......	−5.99(−2)	2.59(+2)	2.50(+2)	2.99
0.133......	−7.08(−2)	2.08(+2)	1.90(+2)	3.10
0.141......	−8.28(−2)	1.69(+2)	1.47(+2)	3.20
0.151......	−9.65(−2)	1.38(+2)	1.15(+2)	3.29
0.161......	−1.12(−1)	1.14(+2)	9.04(+1)	3.38
0.170......	−1.29(−1)	9.46(+1)	7.17(+1)	3.46
0.180......	−1.48(−1)	7.89(+1)	5.71(+1)	3.54
0.189^-....	−1.71(−1)	6.59(+1)	4.55(+1)	3.61
0.189^+....	−2.21	9.42	0	3.61

NOTE.—Units are given in eqs. (2.9) and (3.2), with $\rho_H \rightarrow \Omega_b \rho_H$. The potential is given by the collisionless infall similarity solution.

thus is unstable to collapse (Chandrasekhar 1967). If the gas is not self-gravitating, however, it is stable for smaller values of γ. These results are usually stated for a hydrostatic mass distribution, but they hold also for the self-similar distributions considered here. The difference is that solutions with the form (3.12) near the center are more than unstable for a self-gravitating gas with $\gamma < 4/3$; they do not even exist. The similarity solutions are instead characterized in this case by a central collapse. This result suggests that radiative cooling may lead to formation of a black hole in the center (neglecting the details of the collapse) if the flow is self-gravitating and remains spherical. It is satisfying to see these standard results of stellar structure apply here also for cosmological accretion.

As was emphasized during the treatment of a collisionless gas in § IV, in a similarity solution each fluid particle follows the same nondimensional trajectory $\lambda(\xi)$. For a collisionless

TABLE 10

CONSTANTS OF THE $\Omega_b \ll 1$ COLLISIONAL COSMOLOGICAL SELF-SIMILAR ACCRETION SOLUTIONS

Parameter	$\gamma = 5/3$	$\gamma = 3/2$	$\gamma = 7/5$	$\gamma = 4/3$
λ_s	0.3472	0.2794	0.2293	0.1893
ξ_s	0.5689	0.6056	0.6299	0.6476
$r_s/r'_{\rm ta}$......	0.5757	0.4787	0.4014	0.3366
V_1	−1.433	−1.713	−1.967	−2.206
D_1	4.021	5.381	7.103	9.415
M_1	3.799	3.707	3.648	3.605
$\tilde{D}(0)$.......	2.44	3.09	3.68	4.54
$\tilde{P}(0)$.......	2.15	2.72	3.23	4.00
$\tilde{M}(0)$	10.6	12.8	16.0	19.4
$t/E^{\rm a}$	4.78(−4)	7.70(−4)	2.10(−3)	5.92(−3)
u/E.......	1.190	2.50	7.84	27.62
w/E.......	−2.190	−3.50	−8.84	−28.63
$r_\infty/r'_{\rm ta}$	0.43	0.32	0.23	0.20

NOTE.—The potential is given by the $\Omega = 1$ collisionless infall similarity solution.

[a] Here $E \equiv |t + u + w|$.

gas it is necessary explicitly to calculate $\lambda(\xi)$ to handle shell-crossing, which does not occur in a collisional gas. Nonetheless it is instructive to calculate the trajectory in the collisional case as well. For a collisional fluid particle the equation of motion must be modified to include pressure forces. In nondimensional form the equation of motion becomes

$$\frac{d^2\lambda}{d\xi^2} + \frac{7}{9}\frac{d\lambda}{d\xi} - \frac{8}{81}\lambda = -\frac{1}{D}\frac{dP}{d\lambda} - \frac{2}{9}\frac{M(\lambda)}{\lambda^2}; \qquad (5.4)$$

this differs from equation (4.1) only by the addition of the pressure term. If the potential is determined by a collisionless component, as it is in this section, then M should be replaced by M_x.

Equation (5.4) was integrated to obtain the trajectories shown in Figure 4 for a purely collisional ($\Omega = 1$; see § III) gas, plotted in the form $r/r'_{\rm ta}$ vs. $t/t_{\rm ta}$. These trajectories were discussed in § III. Figure 13 shows the trajectories for the $\Omega_b \ll 1$ collisional fluid and may be compared with Figure 4. The results are as expected. The $\gamma = 5/3$ trajectory is changed very little because the collisionless and $\gamma = 5/3$ collisional mass distributions are so similar. The trajectories for $\gamma < 5/3$ do not settle as far inward in the non–self-gravitating case because the binding energy per particle is not increased by compression. Figure 13 verifies that the $\gamma = 4/3$ solution and, by extension, solutions with $\gamma < 4/3$ are well-behaved for $\Omega_b \ll 1$, as discussed above.

VI. DISCUSSION AND CONCLUSIONS

The analytic and semianalytic solutions presented in this paper for secondary infall and accretion should help to clear up some of the confusion that has arisen previously from conflicting numerical and analytic results. The solutions have many applications to, and implications for, galaxy and cluster formation, but this is not the best place to work out the details. Instead, the discussion will be limited to two areas where simple deductions can be drawn from the solutions. It will be left to later work to more thoroughly explore the consequences of the similarity solutions.

a) *Comparison with Similarity Solutions for Holes*

Paper I found similarity solutions for expanding "holes," or "voids," resulting from the nonlinear growth of an initial negative density perturbation in a Friedmann cosmology. While working out the solutions for holes, the author realized that similarity solutions must also exist for the nonlinear growth of initial positive density perturbations, since a sign change does not affect the dimensional analysis underlying the solutions; this realization led to the current work. The similar-

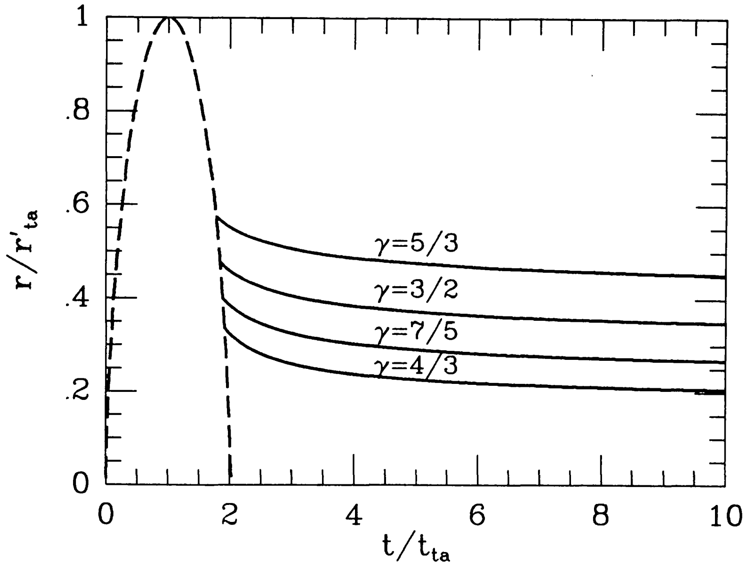

FIG. 13.—Same as Fig. 4, except that the solid curves are for the $\Omega_b \ll 1$ collisional solutions in the potential of the $\Omega = 1$ collisionless similarity solution, and the dashed curve is the first orbit of Fig. 9.

ity solutions for holes are in many ways complementary to the infall solutions given here, so it is natural to compare the two.

The linear evolution of positive and negative perturbations is the same: each grows in magnitude according to equation (1.2), if no initial velocity perturbation is present. The nonlinear evolution is clearly different in the two cases, but the many similarities have not been realized previously. This is largely because holes were assumed to be no more than the absence of matter ("voids"). Only when large holes were discovered in the distribution of galaxies (e.g., Kirshner *et al.* 1981) and numerical simulations were conducted (e.g., Hoffman, Salpeter, and Wasserman 1983), was it realized that holes expand in comoving coordinates; i.e., holes expand more rapidly than $r \sim t^{2/3}$.

An incorrect and naive—but nonetheless helpful—interpretation of the difference between hole expansion and secondary infall is that, while overdense regions "pull" on the matter around them, holes "push" on it. Of course, holes do not really push matter (assuming zero cosmological constant); but they do not decelerate matter, so that when holes appear in a decelerating, expanding cosmological medium (with deceleration parameter q not much less than $1/2$), the effect is as if the nondecelerating mass shells around a hole were pushed out into the surrounding, decelerated matter.

The reason the expansion of holes is of interest here is that, for initial conditions identical with those described in § I, but with the density perturbation having opposite sign (an "uncompensated hole" in the terminology of Paper I), the expansion law for a hole is also given by equation (2.7) for the turnaround radius outside a positive perturbation, up to a constant factor of order unity. This result follows from dimensional analysis and was mentioned above in § II. It follows further that the mass, density, velocity, and pressure (for a collisional gas) scale the same way with time in the two cases. Since the expanding hole sweeps matter up into a thin shell surrounding it, this raises the interesting possibility that a hole may more efficiently compress matter than infall does. This surprising speculation will now be shown to be true.

Consider first a $\gamma = 5/3$ collisional gas: We measure the efficiency in compressing matter by the mass of gas which has been shocked by time t, with identical $|\delta_i|$, R_i, and t_i for the initial positive and negative perturbations. The accretion solution of § III gives the shocked mass

$$m_s^+(t) = \frac{4\pi}{3}\rho_{\rm H} M_2 \left(\frac{3\pi}{4}\right)^{-8/3} \delta_i R_i^3 \left(\frac{t}{t_i}\right)^{8/3}$$

$$= 0.3853\left[\frac{4\pi}{3}\rho_{\rm H}\delta_i R_i^3\left(\frac{t}{t_i}\right)^{8/3}\right]. \qquad (6.1a)$$

From Paper I, the amount of gas in the shocked shell around an uncompensated hole is

$$m_s^-(t) = 0.6072\left[\frac{4\pi}{3}\rho_{\rm H}\delta_i R_i^3\left(\frac{t}{t_i}\right)^{8/3}\right] = 1.576 m_s^+(t). \qquad (6.1b)$$

The ratio of equations (6.1a) and (6.1b) shows that the initial negative density perturbation is 58% more efficient than the positive perturbation in shocking gas.

Next consider a collisionless gas. Here the efficiency of compressing matter is measured by the amount of mass which has passed through at least one caustic by time t. (The collisionless fluid similarity solution for an uncompensated hole has caustics like those in the infall solution.) From § IV, for secondary infall this amount is

$$m_c^+(t) = \frac{4\pi}{3}\rho_{\rm H}\left(\frac{3\pi}{4}\right)^{-2/3} \exp\left(-\frac{2}{3}\xi_1\right)\delta_i R_i^3\left(\frac{t}{t_i}\right)^{8/3}$$

$$= 0.293\left[\frac{4\pi}{3}\rho_{\rm H}\delta_i R_i^3\left(\frac{t}{t_i}\right)^{8/3}\right], \qquad (6.2a)$$

where ξ_1 is given in Table 5. Paper I gives for an uncompensated hole the result

$$m_c^-(t) = 0.3330\left[\frac{4\pi}{3}\rho_{\rm H}\delta_i R_i^3\left(\frac{t}{t_i}\right)^{8/3}\right] = 1.14 m_c^+(t). \qquad (6.2b)$$

The hole is 14% more efficient than infall in compressing collisionless fluid particles through caustics.

The basic reason that uncompensated holes compress matter more efficiently than does infall onto an overdensity is that holes are much larger. The shocks or outermost caustics in the infall solutions occur no farther than about one-third of the turnaround radius from the center (cf. Figs. 2, 3, and 8), while the radius of a self-similar uncompensated hole is about twice the turnaround radius for the corresponding initial positive perturbation. Thus infall strongly affects (through shocks or caustic passage) less than 1% of the volume affected similarly by a nonlinear hole. This point is obviously important for the large-scale structure of the universe. It is interesting that the masses accumulated by infall and hole expansion are actually so similar, considering how different are the sizes. An observational consequence of this is that the largest holes should displace about as much mass as the largest clusters, assuming that both formed from perturbations of the same amplitude on an equal mass scale, but that holes should be several times larger in linear dimension.

The prediction of similar mass scales for holes and clusters is borne out approximately by observations. Rich clusters (e.g., Coma; see Kent and Gunn 1982) have mass $\gtrsim 10^{15}\ M_\odot$, corresponding to uncompensated holes of radius 10–$20 h^{-1}$ Mpc ($h \equiv H_0/100$ km s^{-1} Mpc^{-1}). There are now several holes seen of this size (e.g., Davis *et al.* 1982). But the giant void in Bootes (Kirshner *et al.* 1981), with volume exceeding 10^6 Mpc^3, instead corresponds in mass to a supercluster. Unless this hole is a singular case, the above arguments suggest that superclusters ought to be very nonlinear, in apparent conflict with observations (summarized by Oort 1983).

These results imply that holes, instead of being dynamically "void," may actually dominate the dynamics over that of collapsing overdensities. This conclusion is not without caveats, however. For instance, although the holes are more efficient in sweeping up total mass, much higher mean densities occur in the infall solutions, so gas cooling will be more effective in the infall case for a collisional gas. Also, fragmentation can occur faster in the infall solutions, since the dynamical time scale is given by the Hubble time when a given shell falls in, while the dynamical time is of order the current Hubble time in the shells around holes. However, these arguments cannot disprove equations (6.1) and (6.2). The comparison strongly suggests that any theory of galaxy formation which considers only the growth of initial positive perturbations is sure to make errors of order unity. Considering the poor state of our knowledge about galaxy formation, this may not be important.

b) *Ages of Collisionless Systems*

Similarity solutions generally preserve only that information of a system which is conserved by integrals, e.g., mass and energy. For instance, the exact shape of an initial overdense perturbation cannot be determined after the perturbation collapses and undergoes relaxation, while the total mass excess can be obtained from equation (2.18). It is therefore fortunate that, after undergoing relaxation, the orbit of a collisionless particle is a conserved quantity, for this enables us to obtain the information retained by the particle from earlier times. It is equally fortunate that information about the first turnaround time and radius of the particle is preserved even through relaxation. These facts are illustrated by Figure 9. Not only does the particle orbit become periodic, but its final period and maximum radius can be used to derive its turnaround time and radius. From Table 6, the limiting periodic orbit has a radius about 0.81 times the particle turnaround radius, and period about 1.3 times the particle turnaround time.

We see that the conserved orbital quantities allow a subsystem of a collisionless system formed by secondary infall to be dated. The oldest subsystems are at the smallest radii and have the shortest orbital periods. Younger subsystems are added by secondary infall at successively larger radii. In principle, if the relaxation is of the self-similar form derived in § IV, characterized by the trajectory of Figure 9, most of the dynamical history of an object formed by collisionless infall can be determined.

In the purely self-similar solution this is not of much interest, since infall begins there at $t = 0$ and the object always looks exactly as it does today, only it was smaller in the past. It is actually the deviations from self-similarity, due to the collapse beginning at a finite time and (possibly) infall ending before the present, that are of most interest.

When the collapse first occurs, the similarity solution has not yet been established, so the trajectory is different from that of Figure 9. Qualitatively, during the initial collapse and violent relaxation phase, the orbit shrinks more and its period decreases more than indicated in Figure 9, since at the moment of initial turnaround the system is much farther away from virial equilibrium than equation (4.13) shows the self-similar system to be. Presumably violent relaxation (Lynden-Bell 1967) establishes a $\rho \propto r^{-2}$ profile extending inside the initial turnaround radius, with ρ flattening out inside the core radius. When secondary infall stops much later, the system will already be nearly in virial equilibrium, and the addition of a small amount of mass subsequently will lead to less relaxation for those orbits. The last shells to fall in therefore will hardly be compressed at all. In between these two times, the halo forms in the manner described above, with density distribution $\rho \propto r^{-2.25}$.

Just as the first few orbits after the initial collapse deviate from the self-similar trajectory, the mass, density, and velocity dispersion deviate from the self-similar power-law forms interior to the initial turnaround radius $r_{\rm ita}$. Since self-similar infall adds negligible mass to radii much less than the current turnaround radius (see § IV), the central density is constant long after the initial collapse. (This assumes that collisions are unimportant; after several collisional relaxation times, the central density will again increase.) At larger radii the density scales as $\rho \propto r^{-9/4}$ and is independent of time for $r \ll r_{\rm ta}(t)$. The density in the self-similar halo thus gives a way to estimate the age of the halo. Similar arguments may be carried through for the velocity dispersion; $\sigma \propto r^{-1/8}$ in the similarity solution, but the first shells to collapse have a finite velocity dispersion given after relaxation by the virial theorem, depending on the degree of initial collapse. Care must be used in applying these arguments, since they assume the gas to be purely collisionless and dissipationless, so that no more relaxation occurs than in the similarity solution.

As an example of age determination we estimate the formation (collapse) redshift of halos of large spiral galaxies. Spiral rotation curves are approximately flat for $R > 10$ kpc out to large radii (Rubin, Ford, and Thonnard 1980), indicating that the mass continues to increase with radius, while the disk luminosity falls off exponentially (Freeman 1970). Let us assume that the dark halo matter is collisionless (e.g., faint stars, planets, black holes, or weakly interacting particles), and that the halos are built up by secondary infall. A halo mass shell which now has maximum radius R turned around at radius $r'_{\rm ta} = f^{-1}R$, where $f = 0.8$ (§ IV), at cosmic time $t_{\rm ta}$. We assume that $\Omega \approx 1$ when this shell turned around, even if now $\Omega = \Omega_0 < 1$. This will be valid if the logarithmic slope of the density profile is -2.25 at R. At larger radii, unless $\Omega_0 \approx 1$ and infall continues at present, the density profile will steepen, at the turnaround radius of the last shells to fall in. The mass interior to radius R is (here M is the dimensional mass)

$$M = \frac{2}{9}\frac{M_0 f^{-9/4}}{G t_{\rm ta}^2} R^3, \qquad (6.3)$$

where $M_0 = 11.2$ from equation (4.5). The shell turning around at $t_{\rm ta}$ collapses at $t_{\rm coll} = 2.03 t_{\rm ta}$, giving a collapse redshift of

$$1 + z_{\rm coll} = 2.3\left(\Omega_0 h^2\right)^{-1/3}\left(\frac{M_{12}}{R_{100}^3}\right)^{1/3} = 2.2\,\Omega_0^{-1/3}\left(\frac{V_{200}}{hR_{100}}\right)^{2/3}, \qquad (6.4)$$

where $M = 10^{12} M_{12}\ M_\odot$, $R = 100 R_{100}$ kpc, and $V_{\rm circ} = 200 V_{200}$

km s^{-1} is the circular rotation velocity at R. A similar expression was obtained by Rees and Ostriker (1977). We see that the outer parts of spiral galaxy halos must have collapsed fairly recently. If the halo mass continues to increase beyond 100 kpc, this would be evidence that infall may still be occurring.

Requiring halos to be formed by secondary infall places a lower limit on Ω_0. Suppose a $\rho \propto r^{-2.25}$ profile extends all the way to $R_{\max}$, enclosing mass $M_{\max}$. Then, $\Omega \approx 1$ when the shells interior to $R_{\max}$ collapsed (if $\Omega < 1$, the profile steepens), requiring $1 + z_{\text{coll}} > \Omega_0^{-1}$. Then equation (6.4) gives

$$\Omega_0 > 0.29\left(\frac{M_{\max,12}}{h^2 R^3_{\max,100}}\right)^{-1/2} = 0.30\left(\frac{V_{200}}{hR_{\max,100}}\right)^{-1}. \quad (6.5)$$

Since observations determine V_{circ} versus HR, the h-dependence vanishes from equation (6.5) when observed quantities are used. If Ω_0 is much less than the limit given here, massive halos could not have formed by secondary infall onto a finite mass perturbation.

Unfortunately, dating techniques cannot be used to obtain the age of the central core of a collisionless system, since the initial collapse probably leads to a core radius r_c much less than the initial turnaround radius, with r_c set by the initial velocity dispersion or other factors that are irrelevant to the age. There is clearly much useful information in the central profiles of galaxies and clusters relevant to their formation, but it cannot be deciphered using the similarity solution for secondary infall, which applies instead to the building up of halos.

c) Summary

Similarity solutions have been given in this paper for secondary infall onto an accreting center in an Einstein–de Sitter ($\Omega = 1$) universe. The solutions describe the nonlinear evolution of a spherical positive density perturbation after it collapses. Because the initial density is assumed to equal the critical density outside the perturbation, all mass shells are bound to the perturbation, will eventually stop expanding, and will collapse onto the center. Simple dynamics shows that the turnaround radius, i.e., the distance from the center to the shell halting expansion at time t, grows as $t^{8/9}$ and provides the only scale length in the problem long after the initial collapse, implying the existence of a similarity solution. The problem so stated is undoubtedly a highly idealized picture of the true dynamics in the early universe, but it has the virtue that analytic and semianalytic solutions can be found, whose physical interpretation is relatively straightforward.

The evolution after the initial collapse depends on the central boundary conditions and on the nature of the infalling medium, and this paper is organized to consider the several possibilities. First considered in § II is the case where a black hole lies in the center and swallows all the matter falling onto it, without disturbing the gas. This scenario is chosen partly because of its mathematical simplicity; the collapse is pressureless and without shell-crossing, so analytic solutions can be obtained. But it may describe accretion onto a primeval black hole, and it also gives the motion outside the shell-crossing, or shocked, regions of the other similarity solutions given later.

If there is no central black hole, then infalling fluid elements must either be stopped before reaching the center by passage through a shock, if they are collisional, or pass through the center, if they are collisionless. Section III gives the solutions for shocked accretion of a perfect collisional gas, for which the postshock flow is adiabatic. For a ratio of specific heats $\gamma > 4/3$, the solution has the density profile $\rho \propto r^{-9/4}$ well inside the turnaround radius. For $\gamma = 5/3$ the shock is at a fraction 0.339 of the turnaround radius; for softer equations of state (i.e., smaller values of γ) the shock occurs closer to the center. For $\gamma > 4/3$ collisional fluid particles settle to a fixed distance from the center, explaining the $r^{-2.25}$ density profile in this case. For $\gamma < 4/3$ further collapse occurs in the center (in analogy with the results of stellar structure), with the formation of a black hole likely. This is also the case if radiation is important, so that, e.g., the infalling gas is isothermal.

The similarity solution is given for infall of a collisionless gas in § IV. This turns out to be the most interesting of the cases considered in this paper and is given a fuller treatment than the others. A new Lagrangian technique exploiting the self-similarity of the collisionless particle trajectories is used to obtain the solution without a detailed N-body or shell calculation. It is found that individual particles undergo relaxation over the first few orbits, but then the particle orbits become periodic. The method used to obtain the solution gives the simultaneous motion of all particles, at every phase in the orbits and at every radius. It is found that the relaxation process is self-similar: each new mass shell falling in is virialized and thereafter adds a constant contribution to the resulting power-law density profile $\rho \propto r^{-9/4}$. Relaxation is continual and proceeds to larger radii as new particles turn around at increasing distances from the center. The most interesting result is that the particle orbit becomes periodic after relaxation ceases, a few crossing times after the particle first turns around. The maximum radius of this relaxed orbit is 0.81 times the turnaround radius of the particle. The particle orbit changes so little because the whole system is already largely virialized by the time the evolution becomes self-similar, so the particle sees for the most part a constant force field. The self-similar collisionless mass distribution is found to be surprisingly similar to the $\gamma = 5/3$ collisional distribution of § III.

Caustics, surfaces of cumulative shell-crossing, form in the collisionless solution, and the density is singular at these radii. There is a whole series of caustics, one for every orbit of a particle, but the caustics do not much affect the $r^{-9/4}$ density distribution well inside the turnaround radius. The outer caustics might appear as sharp concentric shells around galaxies or clusters, and observational tests of the secondary infall hypothesis are proposed.

Finite velocity dispersion and angular momentum smear the caustics but do not change the $\rho \propto r^{-2.25}$ density profile. This leads to a nearly flat, circular rotation curve and may be consistent with the rotation curves observed for spiral galaxies.

The density distribution $\rho \propto r^{-9/4}$ resulting from the self-similar relaxation differs from the $\rho \propto r^{-2}$ profile produced by violent relaxation. A partial answer to the question of why is given at the end of § IV.

The existence of similarity solutions does not depend on whether the medium is collisionless or collisional; it may even be composed of both types of particles. Solutions are given in § V for an $\Omega \ll 1$ collisional component moving in the potential of the $\Omega = 1$ collisionless solution derived in § IV. The result differs little from the purely collisional solution of § III if $\gamma = 5/3$, but unlike the self-gravitating collisional case, well-behaved solutions now exist for $\gamma \leq 4/3$, because the gravitational instability leading to collapse for $\gamma \leq 4/3$ occurs only if the gas is self-gravitating.

Finally, §§ VI*a* and VI*b* discuss two consequences of the self-similar infall solutions. The infall solutions are first compared with the self-similar solutions found for the expansion of voids by Bertschinger (1985). Voids form from initial conditions just the opposite of those leading to secondary infall, viz., a negative density perturbation rather than a positive density perturbation. After the negative perturbation becomes nonlinear, a deep hole forms, surrounded by a dense shell. Section VI*a* derives the surprising result that because of the dense shell, a negative perturbation compresses matter somewhat more efficiently than a positive perturbation, suggesting that holes are important initiators of galaxy formation. The amount of mass displaced by a hole is approximately equal to the amount accreted by a cluster forming from an initial perturbation of identical scale and amplitude but opposite sign.

In § VI*b* it is shown that, because particle orbits become periodic in the collisionless infall similarity solution, with the periodic orbit "remembering" the particle's initial conditions, the ages of collisionless systems formed by secondary infall can be determined observationally. Secondary infall builds halos by adding mass at increasing radii; particles at larger radii, with larger periods, fell in most recently. The dating method may be used to obtain the age of collisionless halos, suggesting that massive galactic halos formed recently. A lower limit on Ω_0 follows because infall stops when $\Omega \ll 1$. The dating arguments fail for dissipative systems and for the central parts of collisionless systems, where violent relaxation erases the memory of initial conditions.

This paper is part of a Ph.D. thesis submitted to Princeton University. I would like to thank my thesis adviser, Dr. J. P. Ostriker, for many valuable suggestions. Thanks are also due to Drs. J. R. Gott III and J. E. Gunn for helpful comments. This work was supported in part by a NSF Graduate Fellowship and NSF grants AST 80-22785 and AST 84-13138 and, for publication costs, the University of Virginia.

REFERENCES

Aizu, K. 1973, *Progr. Theor. Phys.*, **49**, 1184.
Bahcall, J. N., Schmidt, M., and Soneira, R. M. 1982, *Ap. J.* (*Letters*), **258**, L23.
Bertschinger, E. 1983, *Ap. J.*, **268**, 17.
______. 1985, *Ap. J. Suppl.*, **58**, 1 (Paper I).
Bondi, H. 1952, *M.N.R.A.S.*, **112**, 195.
Carr, B. J. 1978, *Comm. Ap.*, **7**, 161.
Chandrasekhar, S. 1967, *An Introduction to the Study of Stellar Structure* (New York: Dover).
Chevalier, R., and Imamura, J. 1982, *Ap. J.*, **261**, 543.
Davis, M., Huchra, J., Latham, D. W., and Tonry, J. 1982, *Ap. J.*, **253**, 423.
Dekel, A., Kowitt, M., and Shaham, J. 1981, *Ap. J.*, **250**, 561.
Dekel, A., and Shaham, J. 1980, *Astr. Ap.*, **85**, 154.
Fabian, A. C., Pringle, J. E., and Rees, M. J. 1976, *M.N.R.A.S.*, **175**, 43.
Farouki, R. T., Hoffman, G. L., and Salpeter, E. E. 1983, *Ap. J.*, **271**, 11.
Fillmore, J. A., and Goldreich, P. 1984, *Ap. J.*, **281**, 1.
Freeman, K. C. 1970, *Ap. J.*, **160**, 811.
Goodman, J., and Binney, J. 1983, *M.N.R.A.S.*, **203**, 265.
Gott, J. R. 1975, *Ap. J.*, **201**, 296.
Gunn, J. E. 1977, *Ap. J.*, **218**, 592.
Gunn, J. E., and Gott, J. R. 1972, *Ap. J.*, **176**, 1.
Hoffman, G. L., Salpeter, E. E., and Wasserman, I. 1983, *Ap. J.*, **268**, 527 (HSW).
Hoshi, R. 1973, *Progr. Theor. Phys.*, **49**, 776.
Kent, S. M., and Gunn, J. E. 1982, *A.J.*, **87**, 945.
Kirshner, R. P., Oemler, A., Schechter, P. L., and Shectman, S. A. 1981, *Ap. J.* (*Letters*), **248**, L57.
Lin, C. C., Mestel, L., and Shu, F. H. 1965, *Ap. J.*, **142**, 1431.
Lynden-Bell, D. 1967, *M.N.R.A.S.*, **136**, 101.
Malin, D. F., and Carter, D. 1980, *Nature*, **285**, 643.
Malin, D. F., Quinn, P. J., and Graham, J. A. 1983, *Ap. J.* (*Letters*), **272**, L5.
McCrea, W. H. 1956, *Ap. J.*, **124**, 461.
Oemler, A. 1974, *Ap. J.*, **194**, 1.
Oort, J. H. 1983, *Ann. Rev. Astr. Ap.*, **21**, 373.
Peebles, P. J. E. 1980, *The Large-Scale Structure of the Universe* (Princeton: Princeton University Press).
Pryor, C., and Lecar, M. 1983, *Ap. J.*, **269**, 513.
Rees, M. J., and Ostriker, J. P. 1977, *M.N.R.A.S.*, **179**, 541.
Rubin, V. C., Ford, W. K., Jr., and Thonnard, N. 1980, *Ap. J.*, **238**, 471.
Schweizer, F. 1980, *Ap. J.*, **237**, 303.

EDMUND BERTSCHINGER: Astronomy Department, University of Virginia, P.O. Box 3818, University Station, Charlottesville, VA 22903